1 **Atmospherically-forced sea-level variability in western Hudson Bay, Canada**

3 Igor A. Dmitrenko[1,*], Denis L. Volkov[2,3], Tricia A. Stadnyk[4], Andrew Tefs[4], David G. Babb[1],
4 Sergey A. Kirillov[1], Alex Crawford[1], Kevin Sydor[5], and David G. Barber[1]

7 [1]Centre for Earth Observation Science, University of Manitoba, Winnipeg, Manitoba, Canada

8 [2]Cooperative Institute for Marine and Atmospheric Studies, University of Miami, Miami,
9 Florida, USA

10 [3]NOAA, Atlantic Oceanographic and Meteorological Laboratory, Miami, Florida, USA

11 [4]Department of Geography, University of Calgary, Calgary, Alberta, Canada

12 [5]Manitoba Hydro, Winnipeg, Manitoba, Canada

28 *Corresponding author, igor.dmitrenko@umanitoba.ca, 125 Dysart Rd., University of Manitoba,
29 Winnipeg, Manitoba R3T 2N2 Canada

Abstract: In recent years, significant trends toward earlier breakup and later freeze-up of sea-ice in Hudson Bay have led to a considerable increase in shipping activity through the Port of Churchill, which is located in western Hudson Bay and is the only deep-water ocean port in the province of Manitoba. Therefore, understanding sea-level variability at the Port is an urgent issue crucial for safe navigation and coastal infrastructure. Using tidal gauge data from the Port along with an atmospheric reanalysis and Churchill River discharge, we assess environmental factors impacting synoptic to seasonal variability of sea level at Churchill. An atmospheric vorticity index used to describe the wind forcing was found to correlate with sea level at Churchill. Statistical analyses show that, in contrast to earlier studies, local discharge from the Churchill River can only explain up to 5% of the sea level variability. The cyclonic wind forcing contributes from 22% during the ice-covered winter-spring season to 30% during the ice-free summer-fall season due to cyclone-induced storm surge generated along the coast. Multiple regression analysis revealed that wind forcing and local river discharge combined can explain up to 32% of the sea level variability at Churchill. Our analysis further revealed that the seasonal cycle of sea level at Churchill appears to be impacted by the seasonal cycle in atmospheric circulation rather than by the seasonal cycle in local discharge from the Churchill River, particularly post-construction of the Churchill River diversion in 1977. Sea level at Churchill shows positive anomalies for September-November compared to June-August. This seasonal difference was also revealed for the entire Hudson Bay coast using satellite-derived sea level altimetry. This anomaly was associated with enhanced cyclonic atmospheric circulation during fall, reaching a maximum in November, which forced storm surges along the coast. Complete sea-ice cover during winter impedes momentum transfer from wind stress to the water column, reducing the impact of wind forcing on sea level variability. Expanding our observations to the bay-wide scale, we confirmed the process of wind-driven sea-level variability with (i) tidal-gauge data from eastern Hudson Bay and (ii) satellite altimetry measurements. Ultimately, we find that cyclonic winds generate sea level rise along the western and eastern coasts of Hudson Bay at the synoptic and seasonal time scales, suggesting an amplification of the bay-wide cyclonic geostrophic circulation in fall (October-November), when cyclonic vorticity is enhanced, and Hudson Bay is ice-free.

Keywords: Hudson Bay; sea level; Churchill River discharge; atmospheric vorticity.

1. Introduction

Hudson Bay in northeast Canada is a shallow (mean depth ~ 150 m), semi-enclosed sub-arctic inland sea that is connected to the Labrador Sea through Hudson Strait (Figure 1). The Bay occupies approximately 831,000 km^2, making it the world's largest inland sea, and is characterized by a high annual volume of river discharge (712 km^3; *Déry et al.*, 2005; 2011) and a dynamic seasonal ice cover that exists from November/December to June/July (*Hochheim and Barber*, 2010; 2014). The mean circulation in Hudson Bay is comprised of the wind-driven and estuarine components, where the estuarine portion is driven by the riverine water input (*Prinsenberg*, 1986a), and the wind-driven portion is attributed to prevailing along-shore winds (e.g., *Ingram and Prinsenberg*, 1998; *Saucier et al.*, 2004; *St-Laurent et al.*, 2011; *Ridenour et*

71 *al*., 2019a; *Dmitrenko et al*., 2020). Model simulations by *Saucier et al*. (2004) show that the
72 cyclonic circulation is stronger during fall, reaching a maximum in November when the winds
73 are strongest, and weakest in spring when Hudson Bay has a complete sea-ice cover. *Dmitrenko*
74 *et al*. (2020), however, found that even during the ice covered season strong cyclones can
75 amplify water circulation in the Bay. This is consistent with conclusions by *St-Laurent et al*.
76 (2011), who noted that momentum is transmitted through the mobile ice pack to the water
77 column. The efficiency of momentum transmission through the mobile ice strongly depends on
78 sea-ice roughness, which is impacted by ice concentration and characteristic length scales of
79 roughness elements including pressure ridges, melt ponds etc. (e.g., *Lüpkes et al*., 2012;
80 *Tsamados et al*., 2014; *Joyce et al*., 2019). In particular, ice floes in a state of free drift within a
81 partial or weak ice cover, typical of the polynya area in western Hudson Bay, increase the
82 transfer of wind stress into the water column (*Schulze and Pickart*, 2012). Both velocity
83 measurements (*Prinsenberg*, 1986b; *Ingram and Prinsenberg*, 1998; *Dmitrenko et al*., 2020) and
84 model simulations (*Wang et al*., 1994*; Saucier et al*., 2004; *St-Laurent et al*., 2011; *Ridenour et*
85 *al*., 2019b) show that during summer, cyclonic water circulation produces a coastal transport
86 corridor that advects riverine water along the coast toward Hudson Strait and into the Labrador
87 Sea.

88 The local water mass of Hudson Bay is dominated by freshwater input comprised of river runoff
89 from the largest watershed in Canada and sea-ice meltwater (e.g., *Prinsenberg*, 1984, 1988,
90 1991; *Saucier and Dionne*, 1998; *Granskog et al*., 2009; *Eastwood et al*., 2020). The annual
91 mean discharge rate of 22.6×10^3 m^3 s^{-1} corresponds to a net discharge of 712 km^3 of freshwater
92 per year (*Déry et al*., 2005, 2011). A similar volume of 742 ± 10 km^3 of freshwater is contained
93 within the ice pack by April (*Landy et al*., 2017). Freshwater transport in Hudson Bay exhibits a
94 strong seasonal cycle influenced by the timing of river discharge (e.g., *Déry et al*., 2005), the
95 annual melt/freeze cycle of sea ice (*Ingram and Prinsenberg*, 1998; *Saucier et al*., 2004; *Straneo*
96 *and Saucier*, 2008; *Granskog et al*., 2011), and seasonality of wind forcing (*Saucier et al*., 2004;
97 *St-Laurent et al*., 2011).

98 During the last decade, significant progress has been achieved in understanding the Hudson Bay
99 environmental system (e.g., *Granskog et al*., 2009; *Kuzyk et al*., 2011; *St-Laurent et al*., 2011;
100 *Piecuch and Ponte*, 2015; *Landy et al*., 2017; *Kuzyk and Candlish*, 2019; *Eastwood et al*., 2020;
101 *Dmitrenko et al*., 2020, 2021). However, the synoptic, seasonal, and interannual variability of sea
102 level in Hudson Bay still remains insufficiently studied due to a scarcity of sea level observations
103 at permanent tidal gauges. Note that the tidal gauge in Churchill (Figure 1) is the only
104 continuously operating tide gauge in Hudson Bay and the central Canadian Arctic. Historically,
105 the focus of sea level studies in Hudson Bay was motivated by this area's post-glacial isostatic
106 rebound (e.g., *Guttenberg*, 1941; *Tushingham*, 1992); for a detailed review of these earlier
107 studies see *Wolf et al*. (2006). The advent of space-geodesy, in particular GPS, absolute-
108 gravimetry, and satellite altimetry measurements (e.g., *Larson and van Dam*, 2000; *Wolf et al*.,
109 2006; *Sella et al*., 2007) afforded a shift in focus for Hudson Bay sea level research to
110 environmental aspects related to global warming and hydroelectric regulation (*Gough*, 1998,
111 2000), and those associated with increasing the shipping traffic from the Port of Churchill

112 through Hudson Bay to Hudson Strait, which may soon become a federally-designated
113 transportation corridor (e.g., *Andrews et al.*, 2017; *Pew Charitable Trusts*, 2016).

114 In 2016, the University of Manitoba and Manitoba Hydro launched a project on "Variability and
115 change of freshwater-marine coupling in the Hudson Bay System", named BaySys, which aimed
116 to assess the relative contributions of climate change and river regulation to the Hudson Bay
117 system. Here, we are specifically focused on the impact of the Churchill River diversion on
118 variability of sea level at the Port of Churchill. Additionally, we put our findings in the context of
119 wind forcing over the entire Hudson Bay, elaborating on the suggestion by *Dmitrenko et al.*
120 (2020) that cyclonic wind forcing generates onshore Ekman transport and storm surges along the
121 coast.

122 We also revisit earlier results by *Gough and Robinson* (2000) and *Gough et al.* (2005). Using
123 tidal gauge and river discharge data from 1974 to 1994, *Gough and Robinson* (2000) suggested
124 that the Churchill River discharge dominates sea-level variability at Churchill. They explained
125 the seasonal elevation of sea level during late fall by a recirculating mechanism that links the
126 spring pulse of river discharge in the downstream James Bay (Figure 1) to sea level at Churchill
127 (*Gough and Robinson*, 2000; *Gough et al.*, 2005). In this paper, we present an alternative
128 mechanism and show that (i) the Churchill River discharge plays a secondary role for generating
129 sea level anomalies at Churchill, and (ii) the synoptic and seasonal variability of sea level at
130 Churchill and over the entire Hudson Bay is impacted by the wind forcing described with an
131 atmospheric vorticity index (Figure 2).

132

2. Data

133

134 *2.1. Sea level*

135 The daily mean sea level data used in this study were retrieved from the Canadian Tides and
136 Water Levels Data Archive of the Fisheries and Oceans Canada through http://www.isdm-
137 gdsi.gc.ca/isdm-gdsi/twl-mne/index-eng.htm#s5 (last access: 26 August 2021). Sea level data
138 were de-tided using an algorithm by *Foreman* (1977). Measurements of sea level at Churchill
139 were obtained from the permanent tidal gauge that is installed at the port of Churchill (station
140 #5010) near the mouth of the Churchill River (Figure 1). While measurements of sea level at
141 Churchill date back to the 1930s (*Gutenberg*, 1941), we only used data from 1950 to present
142 (Figure 3a), which is coincident with atmospheric reanalysis data from the National Centers for
143 Environmental Prediction (NCEP; *Kalnay et al.*, 1996). In addition, we used sea level data from
144 the temporary tidal gauge in Innukjuak (station #4575), Cape Jones Island (station #4656), and
145 North Kopak Island (station #4548) (Figure 1). Among these three locations, only data at
146 Innukjuak are fully representative for our analysis because they span a sufficiently long period
147 from October 1969 to October 1980, however, only the portion of this time series from
148 September 1973 to December 1975 is continuous. Sea level records at Cape Jones Island and
149 North Kopak Island are from August-October 1973 and 1975, respectively, and were selected
150 among other temporary stations in Hudson Bay to overlap with sea level time series at
151 Innukjuak.

152 Satellite altimetry data from 1993-2020 were used to analyze the relationship between wind
153 forcing and sea level changes over the entire Hudson Bay. We used the daily fields of absolute
154 dynamic topography (ADT), i.e. the sea surface height above geoid, processed and distributed by
155 Copernicus Marine and Environment Monitoring Service (CMEMS;
156 https://marine.copernicus.eu/; last access: 26 August 2021). The ADT is obtained by adding a
157 mean dynamic topography (DT2018, *Mulet et al.*, 2013) to sea level anomaly (SLA) measured
158 by altimetry satellites. The CMEMS SLA/ADT fields are computed by optimally interpolating
159 data from all satellites available at a given time following a methodology described in *Pujol et
160 al.* (2016). Prior to mapping, altimetry records are corrected for instrumental noise, orbit
161 determination error, atmospheric refraction, sea state bias, static and dynamic atmospheric
162 pressure effects, and tides. Because in this work we are interested in local (dynamic) changes of
163 sea level, the global mean sea level was subtracted from each ADT map. Then the seasonal
164 climatology was computed for Ju~~ne~~ly through August (JJA) and September through November
165 (SON) by averaging all available maps during the respective seasons. Sea ice does not represent
166 a significant problem for computing the climatology, because Hudson Bay is essentially ice free
167 during these months, especially during SON.

168 The root-mean-square differences between tide gauge records and collocated SLA/ADT data are
169 usually 3-5 cm (e.g., *Volkov et al.*, 2007; *Pascual et al.*, 2009; *Volkov et al.*, 2012) and do not
170 exceed 10 cm globally (*CLS-DOS*, 2016). When the altimetry data are averaged to produce the
171 seasonal climatology, the measurement error is greatly reduced (at least by an order of
172 magnitude for 28 years of altimetry record). It should be noted that altimetry errors near the coast
173 are greater than in the open ocean. This is due to land contamination within the radar footprint
174 and to the fact that the geophysical corrections applied to altimetry data are usually optimized for
175 the open ocean and not for the coastal zones. In classical altimetry products, however, a large
176 percentage of data within 10–15 km from the coast is deemed invalid and not used for generating
177 SLA/ADT maps (e.g., *The Climate Change Initiative Coastal Sea Level Team*, 2020).
178 Furthermore, satellite altimetry data was used here only for a qualitative assessment of the basin-
179 scale seasonal sea-level patterns in Hudson Bay. Therefore, the reduced quality of altimetry
180 retrievals near the coast is not expected to impact the conclusions of this study. ~~Sea ice also does
181 not represent a significant problem for computing the climatology, because Hudson Bay is
182 essentially ice free during these months, especially during SON.~~

183 2.2. *River discharge*

184 Churchill River discharge data were obtained from *Déry et al.* (2016) and extended to 2019;
185 thus, we use a continuous record of daily mean discharge from 1960 to 2019 (Figure 4a and
186 supplementary material). The record was constructed from gauged observations above Red Head
187 Rapids (station #06FD001), which is located ~87 km from the Churchill River mouth and is the
188 most downstream hydrometric gauge along the Churchill River. When these data were not
189 available, we used upstream gauges (applying a drainage area correction) to fill significant gaps
190 in the time series (see *Déry et al.* 2005 for detailed methods). Data were adjusted by drainage
191 area (between the hydrometric gauge location and river outlet) and any significant tributary
192 inflows were added to represent discharge at the outlet of the Churchill River.

193   2.3. *Wind forcing*

194   Fields of sea level pressure (SLP) and 10-m wind velocity at 6-h intervals were derived from the
195   NCEP atmospheric reanalysis (https://psl.noaa.gov/data/composites/hour/; last access: 26 August
196   2021). We chose the NCEP reanalysis to extend the atmospheric forcing data back to 1950,
197   which covers the tide gauge record from Churchill, while a previous comparison of wind speeds
198   from NCEP and ERA5 (*Copernicus Climate Change Service*, 2017; *Hersbach et al.*, 2020) with
199   in situ observations from the Churchill weather station revealed an insignificant discrepancy
200   between the two reanalyses and meteorological observations (*Dmitrenko et al.*, 2020). However,
201   we used the ERA5 SLP data to validate atmospheric vorticity derived from NCEP as described
202   below in section 3. For simplicity, cyclones over the Hudson Bay area were manually tracked for
203   August-May 1969-1970 and 2003-2004 using the NCEP SLP fields, with the central position and
204   low SLP tabulated. The horizontal resolution of the NCEP-derived data is 2.5° of latitude and
205   longitude.

206   For the majority of tidal gauge data from 1950s, sea level at Churchill was recorded hourly. In
207   contrast, the Churchill River discharge from gauged observations above Red Head Rapids
208   (station #06FD001) is available daily. The NCEP data on SLP and 10-m wind are available at 6-
209   h intervals. To make these three time series comparable, we analyzed daily means.

210

211   **3. Methods**

212   For the 1950/60–2019 study period, a vorticity index was derived from the daily mean SLP
213   NCEP data to characterize the wind forcing and compare to the time series of sea level anomalies
214   (Figures 2a, 3a, and 4a). The vorticity index gives both the sign and magnitude of atmospheric
215   vorticity; it was first proposed by *Walsh et al.* (1996) and then successfully used for describing
216   atmospheric forcing over the Siberian shelves (*Dmitrenko et al.*, 2008a; 2008b) and Hudson Bay
217   (*Dmitrenko et al.*, 2020). The vorticity index is defined as the numerator of the finite difference
218   Laplacian of SLP for an area within a radius of 550 km centered at 60°N and 85°W in Hudson
219   Bay (Figure 1). A positive index corresponds to cyclonic atmospheric circulation that is typically
220   associated with northerly winds in western Hudson Bay, whereas a negative vorticity index
221   corresponds to anticyclonic atmospheric circulation characterized by southerly winds in western
222   Hudson Bay (Figure 2). *Dmitrenko et al.* (2020) examined the spatial uncertainty of atmospheric
223   vorticity estimated at 60°N, 85°W by computing vorticity for the 5-point stencils with a central
224   node shifted relative to 60°N, 85°W by approximately 280 km northward, eastward, southward,
225   and westward. Their results show that vorticity computed at 60°N, 85°W best describes major
226   cyclonic storms observed in 2016–2017.

227   The vorticity index used in this study does not fully explain the observed variability of
228   meridional wind in western Hudson Bay (Figure 2b), which is mainly responsible for generating
229   storm surge along the coast (*Dmitrenko et al.*, 2020). However, vorticity describes the intensity
230   of cyclonic wind forcing over the entire Bay impacting the basin-scale circulation and sea level
231   deformations along the entire coastline of Hudson Bay (*Dmitrenko et al.*, 2020). Thus, our
232   approach allowed us to extend our findings over the entire Bay. We also conducted a validation

233 comparing the NCEP-derived vorticity to that derived from the ERA5 SLP utilizing the Web-
234 Based Reanalysis Intercomparison Tools (https://psl.noaa.gov/cgi-bin/data/testdap/timeseries.pl;
235 last access: 26 August 2021) described by *Smith et al.* (2014). The comparison showed
236 insignificant differences between the two reanalyses: the NCEP-derived vorticity only slightly
237 exceeds that obtained from ERA5, while the correlation between the NCEP and ERA5-derived
238 vorticities is 0.96 (Figure 2a).

239 The Churchill River discharge time series (Figure 4a) was compiled as follows. First, no
240 significant gaps in Churchill River discharge record occurred on a daily basis. There were,
241 however, some missing discharge data between 1976 and 1995, with some gaps up to 3 months
242 (e.g., 1984, 1987). When data gaps occurred, then the upstream hydrometric gauge below Fidler
243 Lake (station #06FB001) was used to infill data, with streamflow data adjusted to account for the
244 difference in contributing area between Fidler Lake and the Churchill outlet, following the
245 procedure of *Déry et al.* (2005). When the upstream hydrometric data were also unavailable, a
246 secondary step was taken to infill data gaps. Missing data on a given day were infilled using the
247 day-of-year mean value of streamflow over the available period of record. This procedure
248 constructed a daily climatology of streamflow (i.e., mean annual hydrograph) based on the
249 availability of data over the period of record.

250 For the Churchill River, however, we constructed a separate climatology of daily streamflow for
251 the periods prior to and after flow diversion in 1977. Partial diversion began in 1976, allowing
252 less than the full capacity of discharge to be diverted into the Nelson River system, with full
253 operation beginning in 1977. We therefore designated 1977 as the first year when diversion
254 became operational.

255 It is also important to separate the pre- and post-regulation periods for the analysis of the
256 potential impact natural (pre-diversion) and regulated Churchill River discharge have on sea
257 level anomalies at Churchill. *Déry et al.* (2016) reported that the Churchill River diversion
258 caused a significant decline in the mean annual discharge from 37.0 ± 4.2 km^3 year^{-1} pre-
259 diversion (1964–73) compared to post-diversion flows (8.4 ± 2.9 and 9.6 ± 4.4 km^3 year^{-1} for
260 1984–93 and 1994–2003, respectively). *Déry et al.* (2016) further revealed the coefficient of
261 variation (CV) of annual Churchill River discharge increased in inter-decadal CV post-diversion
262 (1984–2013; CV = 0.35–0.67) compared to pre-diversion records (1964–1973; CV = 0.11). Both
263 the decline in mean annual discharge and increase in discharge variability for the post-diversion
264 period necessitate separate analysis of the impact of river discharge on sea level variability due
265 to non-stationarity in the discharge record, which was implemented in our analysis.

266 The sea level record in Churchill is impacted by the post-glacial isostatic adjustment, with
267 present-day uplift in the Hudson Bay area of ~10 mm year^{-1} (e.g., *Sella et al.*, 2007). Combining
268 satellite altimeter data with the Churchill tide-gauge data gives an uplift rate of about 9.0 ± 0.8
269 mm year^{-1} (*Ray*, 2015). The crustal uplift is evident in the negative sea level trend at Churchill of
270 about the same magnitude (Figure 3a). To examine synoptic to seasonal variability of sea level at
271 Churchill, a polynomial fit was subtracted from the data (Figure 3a). The polynomial fit better
272 explains long-term variability of sea level at Churchill compared to the linear approximation,
273 with respective coefficients of determination (R^2) of 0.41 and 39. Thus, in our study we

274   examined the sea level anomalies (SLA) against the low-frequency trend conditioned by the
275   post-glacial isostatic adjustment. In addition, the inverse barometer contribution to the water
276   level record was removed using sea-level atmospheric pressure from the NCEP reanalysis. The
277   mean correction attributed to inverted barometer effect was -1.19 ± 8.72 cm.

278   We used multiple linear regression to estimate a partial contribution of the cyclonic wind forcing
279   and Churchill River discharge to SLA. In this context, multiple regression uses the least squares
280   method to calculate the value of SLA based on the two independent variables as the vorticity
281   index and Churchill River discharge.

282

283   **4. Results**

284   In this section, we examine the impact of wind forcing and local river discharge on sea level
285   variability at Churchill. We analyze (4.1) SLA at Churchill, (4.2) atmospheric vorticity over
286   Hudson Bay, (4.3) the Churchill River discharge, and (4.4) their correlations.

287   4.1. *Sea level*

288   The 30-day running mean of SLA at Churchill ranging from 0.39 m in October 1973 to -0.36 m
289   in April 1981 is dominated by the seasonal cycle (Figure 4a, blue line). In terms of the long-term
290   monthly mean, sea level shows a seasonal cycle with positive anomalies > 0.09 m from
291   September-November and negative anomalies of about -0.14 m from March-April (Figure 5a).

292   There is a substantial difference in the seasonal patterns of sea level between the pre- and post-
293   diversion periods. The long-term variability of sea level (Figure 3a) and SLA (Figure 4a) shows
294   no abrupt disruption with the introduction of the Churchill River diversion in 1977. However, the
295   seasonal cycle of SLA generated for pre- and post-diversion shows a characteristic difference in
296   the timing and magnitude of SLA (Figure 5a). First, for the natural seasonal cycle prior to 1977
297   (blue line in Figure 5a), SLA shows two seasonal peaks in June (~0.04 m; standard error of the
298   mean $\sigma = \pm 0.01$ cm) and November (~0.11 m, $\sigma = \pm 0.02$ cm). Post-diversion, SLA shows no
299   peak in June, but the magnitude of positive anomalies in September and October increased to >
300   0.08 m. This result is consistent with findings by *Gough and Robinson* (2000). In contrast to
301   summer, during February-May, the pre- and post-diversion magnitude of SLA decreased and
302   increased, respectively, by $\geq \pm 0.02$ m relative to the long-term monthly mean (Figure 5a). The
303   standard deviation of the monthly mean values is up to 0.1 m (error bars in Figure 5a). The
304   seasonal pattern of SLA was partially disrupted in 1981-82 and 1987-88, and significantly
305   diminished in 1962-63 and 2016-17 (Figures 3a and 4a).

306   A closer look at the daily data reveals that the sea level seasonal maximum from October-
307   November is modulated by storm surges frequently observed during the late fall. For example, in
308   1969-70 and 2003-04 (highlighted with yellow shading on Figure 4), the seasonal cycle of sea
309   level (Figure 6, thick light blue line) was impacted by synoptic-scale events dominant during
310   October-November (Figure 6, blue line). These storm surges lasted from ~3 to 6 days and
311   correspond to positive anomalies of up to 0.5 m in the daily mean sea level (Figure 6b). In

312 contrast, from December to May, the number and magnitude of storm surges gradually decrease
313 (Figure 6).

314 *4.2. Wind forcing*

315 The vorticity index shows predominant cyclonic atmospheric circulation over Hudson Bay
316 (mostly positive values in Figure 3a, red line), which agrees with results presented by *Saucier et*
317 *al*. (2004) and *St-Laurent et al*. (2011). The strongest positive (cyclonic) vorticity is observed
318 from fall 1962 to winter 1963 (vorticity index exceeded 14 s^{-1}), while the strongest negative
319 (anticyclonic) atmospheric forcing (vorticity < 4 s^{-1}) is recorded during summer 1963 (Figure
320 3a). Overall, the alternation between monthly mean cyclonic and anticyclonic wind forcing is
321 mostly governed by the seasonal cycle in vorticity (Figure 5b). The monthly mean vorticity
322 increases from 4 s^{-1} in September to ~8 s^{-1} in November, and then gradually returns to ~4 s^{-1} in
323 February (Figure 5b). During March-May and August, vorticity is relatively low (< 2 s^{-1}), and
324 only in June and July does vorticity change to weak anticyclonic (slightly negative) values
325 (Figure 5b). The seasonal cycle in atmospheric vorticity shows an insignificant difference pre-
326 and post-diversion. From May to August and in December, there is no difference between the
327 long-term monthly mean and monthly mean estimates for pre- and post-diversion (Figure 5b).
328 For other months, the difference does not exceed ± 0.7 s^{-1}.

329 The interannual variability of wind forcing is mainly attributed to year-to-year changes in the
330 cyclonic atmospheric circulation during fall-winter months. The seasonal amplitude of vorticity
331 is significantly diminished in 1953-54, 2001-02 and 2015-2016 when the seasonal mean vorticity
332 index for late fall to the beginning of winter did not exceed 8 s^{-1} (black triangles in Figure 3a). In
333 contrast, during 1960-65, the vorticity seasonal cycle is amplified with the seasonal mean
334 vorticity index between late fall and early winter up to 28 s^{-1} (green triangles in Figure 3a). The
335 standard deviation of the monthly mean vorticity shown by error bars in Figure 5b gradually
336 decreases from ± 4.5 s^{-1} in December to ± 2.8 s^{-1} in March-April.

337 Analysis of the daily vorticity time series sheds light on the origin of seasonality in vorticity.
338 Positive seasonal anomalies from September-December (Figures 3a and 5b) are partly attributed
339 to the occurrence of numerous vorticity peaks. For example, in 1969-70 and 2003-04
340 (highlighted with yellow shading in Figure 3), the seasonal enhancement of atmospheric vorticity
341 (Figure 6, thick pink line) was partially conditioned by synoptic-scale events recorded during
342 October-November 1969 and 2003 (Figure 6, red line). The strongest vorticity peaks were
343 observed on 18 October and 25 November 1969 (>4 s^{-1}; Figure 6a) and 15 October and 21
344 November 2003 (>5 s^{-1}; Figure 6b). The SLP spatial distribution reveals that each of these peaks
345 is attributable to a cyclone passing over Hudson Bay, with the center of low SLP located over the
346 central Hudson Bay on 18 October and 25 November 1969 (Figures 7a and 7b, respectively) and
347 15 October and 21 November 2003 (Figures 7c and 7d, respectively). The horizontal gradients of
348 SLP over western Hudson Bay ranged from 0.020 hPa km^{-1} (25 November 1969; Figure 7b) to
349 0.035 hPa km^{-1} (21 November 2003; Figure 7d). Overall, from 1 September to 31 December,
350 vorticity exceeded 2 s^{-1} nine and 12 times in 1969 and 2003, respectively. In contrast, from 1
351 January to 30 April 1970 and 2004, vorticity exceeded 2 s^{-1} only four and seven times,

352 respectively (Figure 6). This suggests that the seasonal cycle in atmospheric vorticity is partially
353 governed by the number and strength of cyclones passing over Hudson Bay.

354 4.3. *Local river discharge*

355 The time series of Churchill River discharge (Figure 4a) is dominated by (i) the introduction of
356 the flow diversion in 1977 and (ii) the seasonal hydrologic cycle. The mean discharge dropped
357 by about one-third from 1,190 m^3 s^{-1} (1960-1976) to about 400 m^3 s^{-1} following the diversion in
358 1977. At the same time, the standard deviation of the mean discharge increased from about ±300
359 to ±470 m^3 s^{-1} following the diversion (Figure 4a). This is in line with results by *Déry et al*.
360 (2016). The mean annual timing of maximum river discharge during late spring to summer is not
361 significantly disrupted by the diversion (Figure 5c). The magnitude of the monthly mean
362 discharge pre- to post-diversion, however, reduces from about five-fold in March to about two-
363 and-a-half-fold in May-August (Figure 5c). After diversion, the standard deviation of the
364 monthly mean discharge doubles from May to October (Figure 5c). In contrast, from December
365 to April, the standard deviation of the monthly mean was not significantly impacted by the
366 diversion (Figure 5c).

367 4.4. *Sea level response* to *wind forcing and local river discharge*

368 Our data shows that SLA in Churchill, atmospheric vorticity over Hudson Bay, and Churchill
369 River discharge all show variability dominated by the seasonal cycle (Figures 3a, 4a, and 5). In
370 what follows, SLA at Churchill is first compared to the atmospheric vorticity, and then to the
371 Churchill River discharge, with a main focus on the seasonal cycle.

372 The correlation between the daily vorticity index and SLA from 1950-2019 and 1960-2019 is
373 0.48 and 0.47, respectively, with insignificant differences between correlations estimated for
374 periods pre- and post-diversion (0.49 and 0.47, respectively; Figure 3b and Table 1). For the ice-
375 free period from June to November, correlations for whole period, and pre- and post-diversion
376 increase to 0.54, 0.52 and 0.55 (Table 2), respectively, compared to 0.47, 0.49 and 0.47 for the
377 ice-covered period from December to May (Table 3). We test the difference between correlations
378 estimated for the ice-covered and ice-free seasons using the Fisher z-transformation (*Fisher*,
379 1921). Statistical assessment shows that the only differences between correlations estimated for
380 whole period and post-diversion are statistically significant at the 99% confidence level.

381 The relationship between vorticity and SLA changes significantly from one year to another. The
382 mean annual correlations in Figure 3b show these differences ranging from 0.18 in 1982 to 0.69
383 in 1991. During periods when the sea level seasonal cycle almost disappears (1981-82 and 1987-
384 88), the mean annual correlation drops to about 0.3 and 0.4, respectively (Figure 3b). When the
385 sea level seasonal cycle is diminished (1962-63 and 2016-17), a modest correlation of ~0.5 is
386 estimated (Figure 3b). For time periods enlarged in Figure 6, the annual mean correlation
387 significantly exceeds the long-term mean of 0.47, attaining 0.65 and 0.57 for 1969-70 and 2004-
388 05, respectively (Figure 3b). The direct linkage between vorticity and SLA is evident in Figure 6.
389 During September-November 1969 and 2003, all significant synoptic peaks in SLA are
390 consistent with those in atmospheric vorticity, including storm surges on 18 October and 25
391 November 1969 (Figure 6a) and on 15 October and 21 November 2003 (Figure 6b).

392 In contrast to atmospheric vorticity, the correlation between daily SLA and river discharge is
393 significantly smaller. Through the full record from 1960 to 2019, the correlation is 0.22, with an
394 insignificant difference between pre- and post-diversion (0.20 and 0.23, respectively, Figure 4b
395 and Table 1). For the ice-free period from June to November, correlations drop close to or below
396 the level of statistically significant values for the whole and pre-diversion periods (0.08 and 0.03,
397 respectively), and to 0.11 post-diversion (Table 2) compared to 0.21, 0.12 and 0.19 for the ice-
398 covered period from December to May (Table 3). Note that the difference between correlations
399 estimated for the ice-covered and ice-free seasons is statistically significant for only 1960-2019.

400 Similar to the linkage between vorticity and SLA, the relationship between river discharge and
401 SLA shows significant interannual variability. Correlations computed through the 365-day
402 moving window show negative to positive values ranging from -0.3 to 0.7 with about 15% of
403 estimates below the level of statistical significance (Figure 4b). Among all events when the
404 amplitude of the sea level seasonal cycle was strongly reduced, only 1962-63 and 1981-82 show
405 statistically significant correlation between river discharge and SLA of ~0.25 (Figure 4b). For
406 events in 1987-88 and 2016-17, correlation is relatively close to or below the level of statistical
407 significance (Figure 4b). The interannual difference in contribution of river discharge to the sea
408 level variability is also evident for 1969-70 and 2004-05. In 1969-70, the annual mean
409 correlation shows relatively modest contributions of river discharge to sea level variability
410 (correlation R~0.29; Figure 4b) as compared to correlation with atmospheric vorticity (R~0.65;
411 Figure 3b). In 2004-05, however, there is no correlation between SLA and river discharge
412 (Figure 4b), and sea level variability is impacted by wind forcing ($R = 0.57$; Figure 3b).

413 Overall, our results show that the wind forcing impacts the synoptic and seasonal variability of
414 sea level. In what follows, we use the coefficient of determination (R^2, where R is correlation
415 coefficient in Tables 1-3) to describe the proportion of the variance in sea level that is explained
416 by the wind forcing, river discharge, and the wind forcing and river discharge together. Through
417 the whole annual cycle from 1960 to 2019, wind forcing explains about 22% of sea level
418 variability, while river discharge contributes only ~5%. Multiple regression analysis shows that
419 on average, both explain ~28% of sea level variability (Table 1).

420 Our results also reveal the important role of sea-ice cover and river diversion in modifying
421 controls on sea level variability. During the ice-free seasons from 1960-1976, the contribution of
422 wind forcing is 27%, and the role of river discharge is negligible (Table 2). Post-diversion,
423 cyclonic wind forcing and river discharge contribute 30% and 1%, respectively. Together they
424 explain up to 32% of sea level variability (Table 2). During the ice-covered season, the
425 contribution of vorticity is reduced to 22%, with insignificant difference between pre- and post-
426 diversion (Table 3). The contribution of river discharge varies from 1% for pre-diversion to 4%
427 for post-diversion. Wind and river forcing together explain ~27% of sea level variability for both
428 pre- and post-diversion periods (Table 3). Summarizing these results, we point out that the sea-
429 ice cover reduces the influence of wind forcing, and the influence of local river discharge is
430 slightly increased primarily during the ice covered post-diversion period. Post-diversion, the
431 magnitude of river discharge was reduced about three-fold, but seasonal variability increased by
432 a factor of 1.5 (Figure 4a and *Déry et al*., 2016). Thus, we attribute the increase in river

433   discharge forcing during the post-diversion period mainly to the higher variability in river
434   discharge from May to November (Figure 4a, 5c, and *Déry et al.*, 2016). Note that during May
435   about 85% of Hudson Bay is ice covered (*Tivy et al.*, 2010), and the standard deviation of the
436   monthly mean discharge in May increases from about ±170 pre-diversion to ±380 m^3 s^{-1} post-
437   diversion.

438

439   **5. Discussion**

440   Our results show that sea level variability at Churchill is rather influenced by wind forcing, with
441   discharge from the Churchill River playing a secondary role. Overall, the atmospheric vorticity
442   explains up to 30% of sea level variability at Churchill, with local river discharge contributing up
443   to only 5% (Tables 1-3). This suggests that in western Hudson Bay the northerly winds
444   associated with cyclonic wind forcing (Figure 2b) generate storm surge along the coast due to a
445   surface Ekman on-shore transport. This is consistent with results from *Dmitrenko et al.* (2020),
446   who used mooring records and Churchill tide gauge observations in 2016-17 to identify this
447   mechanism. A direct response of the water level to balance wind stress acting on the surface does
448   not play a role for generating SLA because there is no correlation between SLA and zonal wind
449   (not shown).

450   The SLA seasonal cycle in Figure 5a is only partially explained by seasonality in wind forcing
451   and local river discharge. The SLA seasonal cycle is also consistent with summertime warming
452   and freshening, and wintertime cooling and salinification. During the ice-free summer period, the
453   water column warms, and seawater becomes less dense and expands, causing the thermosteric
454   sea-level rise. In addition, during summer, riverine water and sea-ice meltwater decrease salinity
455   of the Bay, thus, causing the halosteric sea-level rise. It seems that these factors can explain the
456   significant fraction of the SLA seasonal variability that is not explained by wind forcing and
457   local river discharge. However, the detailed assessment of the thermosteric and halosteric
458   contributions to the Hudson Bay sea level variability is beyond the scope of this paper. In this
459   context, we point out that we examine only the direct impact of the river discharge on the sea
460   level in the Churchill River mouth ignoring the cumulative effect of riverine water on steric
461   height. This simplification seems to be reasonable because the residence time of the riverine
462   water fraction in southwestern Hudson Bay during summer is ~1-3 months (*Granskog et al.*,
463   2009).

464   For the seasonal time scales, increased cyclonic activity during fall to early winter impacts the
465   seasonal cycle in SLA. In contrast to *Gough and Robinson* (2000), we assert that a positive SLA
466   from September-November (Figure 5a) is attributed to enhanced atmospheric vorticity rather
467   than to the local river discharge. The signature of the local river discharge is, however, traceable
468   through the SLA seasonal cycle. During the pre-diversion period, positive SLA in June (Figure
469   5a) appears to be linked to the spring freshet of the Churchill River (Figures 5a and 5c).
470   However, post-diversion this positive SLA in June vanishes due to the abrupt decrease in the
471   Churchill River discharge during the spring freshet from ~1,500 to 700 m^3 s^{-1} (Figure 5c).
472   Gradual decreases in Churchill River discharge from June/July to April for both pre- and post-

473 diversion cannot explain the positive SLA from fall to winter, especially during the post-
474 diversion period when the mean annual Churchill River discharge decreases to ~400 m^3 s^{-1}
475 (Figure 5c). Note that the cumulative effect of riverine water on steric height is neglected.

476 An additional perspective on SLA response to atmospheric and river forcing comes from a
477 comparison of the monthly mean vorticity and Churchill River discharge time series$^{\text{?}}$ with SLA
478 at Churchill for the whole period of river discharge observations, and the pre- and post-diversion
479 periods (Figures 8a, 8b, and 8c, respectively). The SLA patterns for the whole period of river
480 discharge observation (Figure 8a) are strongly impacted by changes in the magnitude of
481 discharge during the pre- and post-diversion periods, as previously discussed. In contrast, the
482 SLA patterns compiled for the pre- and post-diversion periods (Figures 8b and 8c, respectively)
483 provide more precise features of the SLA response to atmospheric and river forcing. In general,
484 comparing atmospheric vorticity to sea level at Churchill shows that cyclones generate positive
485 SLA up to 0.15 m (Figure 8c). The maximum SLA response to cyclonic atmospheric forcing is
486 observed during the ice-free period (pink shading and white circles in Figures 8b and 8c), which
487 is consistent with results of the correlation analysis (Tables 2 and 3). The combination of
488 anticyclonic (negative) vorticity and low river discharge generates negative SLA up to 0.09 m
489 during both ice-free and ice-covered seasons (blue shading in Figures 8b and 8c).

490 The zero SLA contour in Figure 8b and 8c is displaced relative to the zero vorticity and the long-
491 term mean river discharge for the pre- and post-diversion periods. This indicates that these two
492 predictors alone are insufficient to entirely explain the sea level variability, and that there must
493 be other contributing factors. Correlation analysis (Tables 2 and 3) suggests that sea-ice also
494 plays a role in modifying the impact of atmospheric forcing on SLA. In this context, Figures 8
495 reveals the role of sea-ice cover for generating the SLA. The sea level at Churchill exhibits
496 negative SLA while atmospheric vorticity is positive, but not exceeding ~6-8 s^{-1} (Figure 8). This
497 situation is usually observed during the ice-covered season when river discharge is below the
498 annual mean (blue circles and blue shading in Figures 8b and 8c). We attribute this disruption to
499 the sea-ice cover. Throughout the entire year, positive SLA is generated in response to strong
500 cyclones with vorticity exceeding ~6-8 s^{-1} regardless of the river discharge contribution and sea-
501 ice conditions (red shading in Figure 8 for vorticity >~6-8 s^{-1}). During the ice-covered season, at
502 relatively low river discharge (<1,200 m^3 s^{-1} and 350 m^3 s^{-1} for pre- and post-diversion,
503 respectively), negative SLA is associated with positive vorticity <6-8 s^{-1} (blue circles and blue
504 shading in Figures 8b and 8c). Thus, vorticity ~6-8 s^{-1} is suggested to be a very rough estimate of
505 the vorticity threshold attributed to the sea-ice impact. Above this threshold, sea-ice does not
506 eliminate wind stress from the water column, and wind forcing impacts sea level variability in
507 Churchill year-round. Below this threshold, sea-ice eliminates wind forcing and a negative SLA
508 is conditioned by low river discharge. In fact, extension of the landfast ice as well as sea-ice
509 roughness and concentration can play a role modifying the thresholds at which wind impacts the
510 SLA. When the Churchill River discharge exceeds the monthly means of 1,500-1,600 m^3 s^{-1} and
511 ~900 m^3 s^{-1} for pre- and post-diversion periods, respectively, positive SLA results regardless of
512 wind forcing.

513 Our results on the mechanisms of sea level variability at Churchill differ from those obtained by
514 *Gough and Robinson* (2000). First, using sea level and river discharge data from 1974-1994, they
515 found that correlation between Churchill River discharge and SLA in Churchill explains 43% of
516 sea level variability (versus the 5% derived in our analysis). Second, *Gough and Robinson*
517 (2000) explain a positive SLA observed in Churchill from October-November by the river
518 discharge pulse into the James Bay region with an advective lag of ~4-5 months. Furthermore,
519 *Gough et al.* (2005) speculate that positive SLA during fall is attributed to the James Bay
520 riverine water fraction, which does not exit the Bay through Hudson Strait, but instead re-
521 circulates in western Hudson Bay. The halosteric sea level changes associated with this
522 freshwater fraction are suggested to generate a positive SLA observed in Churchill from
523 October-November. The pathway of this water and the reason for disrupting the mean cyclonic
524 circulation in the Bay were, however, neither specified in *Gough and Robinson* (2000) nor in
525 *Gough et al.* (2005). The distance from James Bay to Churchill measured along the coast is
526 roughly 1,000 km. For a 120-150-day lag between peaks in river discharge to James Bay in June
527 (*Déry et al.*, 2005) and maximum positive SLA at Churchill in November, this distance suggests
528 the unrealistic rate of mean advective velocity to be ~8-10 cm s^{-1}. Note that *Dmitrenko et al.*
529 (2020) estimated the velocity of the northward flow along the western coast of Hudson Bay
530 during strong cyclonic storms to ~13 cm s^{-1}, which significantly exceeds the annual mean
531 meridional transport of ~1-2 cm s^{-1}.

532 Overall, the hypothesis by *Gough and Robinson* (2000) and *Gough et al.* (2005) about the
533 linkage between the river discharge pulse into James Bay and a positive SLA in Churchill is
534 suggestive of the seasonal disruption of the Hudson Bay cyclonic circulation that is in line with
535 the seasonal pattern of atmospheric vorticity in Figure 5b. Based on satellite altimetry and
536 numerical simulation, *Ridenour et al.* (2019a) revealed a seasonal reversal to anticyclonic
537 circulation in southwestern Hudson Bay from May-July, with a return to strong cyclonic
538 circulation in fall in response to the seasonal patterns of surface stress. This is consistent with the
539 seasonal cycles of vorticity presented in Figure 5b. However, among ~120-150 days of the
540 hypothetical transit time from James Bay to Churchill, the anticyclonic atmospheric forcing is
541 persistently observed only during May-July; in August, vorticity returns to cyclonic (Figure 5b).
542 In the three months before the occurrence of the positive SLA at Churchill in November, the
543 atmospheric forcing has already retuned to cyclonic (Figure 5b). In this context, the hypothesis
544 by *Gough and Robinson* (2000) and *Gough et al.* (2005) linking SLA in Churchill to river
545 discharge in James Bay seems to be inconsistent. In what follows, we provide additional
546 arguments to support our finding on the role of wind forcing in generating the SLA at Churchill.

547 First, *Tushingham* (1992) provide the time series of sea level at Churchill and the Churchill River
548 discharge from 1972 to 1989 (Figure 5 from *Tushingham*, 1992). These time series[2] clearly show
549 an overall low positive correlation completely disrupted in 1973-74, 1977, and 1987-86, which is
550 consistent with our analysis (Figure 4). For 1973-74 and 1987-86, the annual-mean correlation
551 was estimated to be about –0.1 and is below the level of statistical significance (Figure 4b).
552 Overall, from 1960 to 2019, there were 19 events that lasted up to 1.8 years in duration when
553 correlations between the SLA and river discharge were statistically insignificant or even negative
554 (Figure 4b). This calls into question the correlations between Churchill River discharge and SLA

555   in Churchill reported by *Gough and Robinson* (2000) and *Gough et al.* (2005). Note that the
556   period from 1972 to 1989 used by *Tushingham* (1992) overlaps with the majority of the period
557   from 1974 to 1994 used by *Gough and Robinson* (2000).

558   Second, *Ward et al.* (2018) analyzed daily data from the Global Runoff Data Centre for 187
559   stations including Churchill and daily maxima sea level data from the Global Extreme Sea-level
560   Analysis. They found no statistically significant dependence between annual maxima of the
561   Churchill River discharge and sea level. For comparison, along the Pacific coast of North
562   America, the correlation ranged from 0.2 to 0.4, and accounted for 4-16% of the variation in sea
563   level. This is consistent with a previous concern about significant impact of Churchill River
564   discharge on SLA in Churchill.

565   Third, our analysis shows that the seasonal cycle in sea level variability with positive SLA
566   during fall is observed not only in Churchill, but also along the eastern coast of Hudson Bay in
567   Innukjuak (Figures 1 and 9). While the sea level record at Innukjuak is short and not continuous,
568   a positive SLA is recognizable during fall 1969-70 and 1973-76 (Figure 9, blue line). Note that
569   the seasonal SLA at Innukjuak cannot be generated locally because the annual mean (1964-2000)
570   discharge of the local Innuksuak River is only 3.3 km^3 year^{-1}, about three times smaller than the
571   Churchill River discharge post-diversion (*Godin et al.*, 2017). In contrast, the seasonal pattern in
572   SLA at Innukjuak is generated by the same cyclonic forcing as in Churchill. Seasonal SLA in
573   Innukjuak is consistent with seasonal amplification of atmospheric vorticity (Figures 5b and 9).
574   Moreover, in Innukjuak, the sea level peaks on 18 October and 25 November 1969 are coherent
575   with peaks in atmospheric vorticity (Figure 9) and sea level at Churchill (Figure 6a). From the
576   preceding analysis we explicitly know that these two vorticity peaks were generated by cyclones
577   passing over the Bay (Figure 7a). The coherent peaks in sea level in Churchill and Innukjuak
578   suggest that cyclones that were centered over Hudson Bay on 18 October and 25 November 1969
579   generated storm surge on both the eastern and western coasts of Hudson Bay. This is also
580   supported by a coherent response of sea level to atmospheric forcing at Cape Jones Island and
581   North Kopak Island (Figures 1 and 9). Our hypothesis is also consistent with results of sea level
582   numerical simulations in response to cyclones passing over the Bay in 2016-17 (*Dmitrenko et al.*,
583   2020). For synoptic storm surges, on-shore Ekman transport increases the mass of water column
584   along the coast (the barotropic component). The seasonal baroclinic component appears during
585   summer when water is fresher and warmer causing the thermosteric and halosteric sea-level rise
586   along the coast.

587   Fourth, satellite altimetry reveals a spatially uniform response of sea level to the seasonal cycle
588   in atmospheric vorticity along the whole coast of Hudson Bay (Figure 10). For 1993-2020, we
589   examine the difference between the sea surface heights (SSH) during summer, when monthly
590   mean atmospheric vorticity changes from –0.7 s^{-1} in June to 1.1 s^{-1} in August, and fall, when
591   vorticity increases from 4.2 s^{-1} in September to 7.3 s^{-1} in November (Figure 5b). Results suggest
592   that enhanced cyclonic vorticity during fall generates seasonal SSH elevation over the entire
593   coast of Hudson Bay with SSH differences between fall and summer ranging from >5 cm in
594   James Bay to ~1 cm along the northwest coast (Figure 10). This confirms our results that a
595   positive SLA during fall is generated over the entire coast of Hudson Bay, and particularly in

596   Churchill and Innukjuak, in response to enhanced cyclonic wind forcing (Figures 5a, 5b, and 9).
597   Overall, our third and fourth points suggest that the hypothesis of *Gough and Robinson* (2000)
598   and *Gough et al.* (2005) about a linkage between river discharge into James Bay and SLA in
599   Churchill is inconsistent.

600   One may suggest that seasonal SSH elevation in Figure 10 can be partly due to the thermosteric
601   and halosteric sea-level rise. During summer, the Hudson Bay coastal domain receives large
602   amount of fresh and warm water from river runoff. The seasonal tendency for river discharge,
603   however, is opposite to that for the SSH in Figure 10. For 1988-2000, *Déry et al.* (2005) reported
604   that the total discharge of rivers flowing into Hudson Bay peaks in June at ~3.6 km^3 day^{-1}, which
605   significantly exceeds the secondary maximum in October (~2.3 km^3 day^{-1}). The seasonal mean
606   total river discharge in September-November (~1.9 km^3 day^{-1}) is one-and-a-half times smaller
607   compared to ~2.8 km^3 day^{-1} in June-August. Based on these estimates, the river discharge
608   seasonal cycle in June-November is inconsistent with that for the SSH in Figure 10. The
609   cumulative effect of river discharge on the seasonal cycle can play a role, but the residence time
610   of the riverine water fraction in southwestern Hudson Bay during summer is relatively small (~1-
611   3 months; *Granskog et al.*, 2009).

612   Finally, our results on the atmospheric forcing of the Hudson Bay SLA are in agreement with
613   conclusions by *Piecuch and Ponte* (2014, 2015). Using ocean mass measurements from satellite
614   gravimetry conducted during the Gravity Recovery and Climate Experiment, they found that
615   wind forcing dominates sea-level and mass variability in Hudson Bay, and wind might drive
616   Hudson Bay mass changes due to wind-driven outflow through Hudson Strait (*Piecuch and*
617   *Ponte*; 2014). For the sea level interannual variability in Hudson Bay, also evident in Figure 4a,
618   *Piecuch and Ponte* (2015) revealed a wind-driven barotropic fluctuation that explains most of the
619   non-seasonal sea level variance. Furthermore, they suggest that anomalous inflow and outflow
620   through Hudson Strait, which impacts sea level variability in Hudson Bay, are driven by wind
621   stress over Hudson Strait. This highlights the role of wind forcing in amplifying the freshwater
622   outflow from Hudson Bay, as also suggested by *Straneo and Saucier* (2008) and *Dmitrenko et al.*
623   (2020).

624   In summary, we suggest that seasonal amplification of atmospheric vorticity, partially
625   conditioned by the number and strength of cyclones passing over the Bay during fall to early
626   winter, generates the seasonal cycle in sea level variability over the entire Bay as depicted
627   schematically in Figure 11. Cyclones passing over Hudson Bay during fall to early winter cause
628   on-shore Ekman transport and storm surges over the entire coast of Hudson Bay (Figure 11a). In
629   summer, anticyclonic wind forces off-shore Ekman transport lowing sea level along the coastline
630   of Hudson Bay (Figure 11b).

631

632   **Summary and conclusions**

633   Our analysis revealed that in contrast to previous research, the local Churchill River discharge
634   explains only up to 5% of the sea level variability at Churchill. Cyclonic atmospheric forcing is
635   shown to explain from 22% during the ice-covered winter-spring season to 30% during the ice-

636   free summer-fall season (Tables 1-3). Multiple regression analysis showed that atmospheric
637   forcing and local river discharge together can explain up to 32% of the sea level variability at
638   Churchill. We found that a positive sea level anomaly in Churchill during fall is partially
639   conditioned by the seasonal cycle in atmospheric vorticity, with prevailing cyclonic wind forcing
640   during fall to the beginning of winter (Figure 5). Sea-ice cover reduces wind stress on the water
641   column during the ice-covered season from December to May, and cyclonic wind forcing
642   generates positive sea level anomalies at Churchill when only the monthly mean vorticity
643   exceeds ~6-8 s^{-1} (Figure 8). In this context, transition towards a longer open water season (e.g.,
644   *Hochheim and Barber*, 2014) is expected to increase the contribution of atmospheric forcing to
645   sea level variability.

646   We expanded our observations at Churchill to the bay-wide scale using sea level observations
647   along the eastern coast of the Bay and satellite altimetry. A coherent sea level response to
648   atmospheric forcing observed at the opposite sides of Hudson Bay suggests that the spatial scale
649   of cyclones passing over Hudson Bay roughly equals the Hudson Bay area (Figures 7 and 9, and
650   *Dmitrenko et al.*, 2020). This scaling equivalency implies that cyclones passing over Hudson Bay
651   cause on-shore Ekman transport and storm surges over the entire Hudson Bay coast (Figure 11a).
652   This is also consistent with results by *Dmitrenko et al.* (2020) obtained for 2016-17. Moreover,
653   the satellite altimetry data shows that this scaling equivalency works not only for synoptic, but
654   also for the seasonal time scale. The seasonal cycle in atmospheric vorticity (Figure 5b) partially
655   conditions the seasonal cycle in sea level variability over the entire coast of Hudson Bay. The
656   recurring cyclonic wind forcing during fall favors sea level elevation over the entire Hudson Bay
657   coast compared to summer (Figures 10 and 11). This seasonal pattern in sea-level variability
658   seems to have implication for geostrophic circulation. The cross-shelf pressure gradient
659   generated due to seasonal amplification of sea level along the coast drives alongshore
660   geostrophic flow and favors the cyclonic circulation around Hudson Bay during fall to earlier
661   winter. In contrast, during summer the geostrophic component attributed to the anticyclonic
662   atmospheric forcing disrupts the Hudson Bay cyclonic circulation as shown by *Ridenour et al.*
663   (2019a).

664   Our research is important for maritime activity within the Bay. Communities around the Bay
665   ~~highly~~ rely heavily on the annual summer sea-lift to re-supply them at a fraction of the price
666   compared to air transport (*Kuzyk and Candlish*, 2019). In this context, positive coastal sea level
667   anomalies during fall favor re-supply operations to coastal communities. However, increased
668   cyclonic activity during fall is also associated with extreme wind events (Figure 2b) and storm
669   surges (e.g., Figure 6) increasing risks to re-supply and fuel-transfer operations.

670   The origin of seasonality in wind forcing, its climatic aspects and ocean response to seasonal and
671   interannual variability in atmospheric vorticity over the Bay are among important priorities for
672   our future research. The freshwater storage in Hudson Bay and export through Hudson Strait
673   seem to be directly impacted by seasonal and interannual variability in wind forcing, clearly
674   defining the need for further research in this area using multi-year numerical simulations and
675   atmospheric reanalyses. Seasonality of the wind forcing is the hypothesized cause of the sea
676   level variability, but probably does not provide a complete explanation. The steric changes in

677 coastal zone attributed to river runoff were not taken into account that points out a necessity for
678 future research involving numerical simulations. Possible impacts of climate change on cyclone
679 activity in Hudson Bay, and therefore sea-level variability, will be addressed in future research.

680

681 **Data availability**

682 Sea level data used in this study are available from the Canadian Tides and Water Levels Data
683 Archive of the Fisheries and Oceans Canada through http://www.isdm-gdsi.gc.ca/isdm-gdsi/twl-
684 mne/index-eng.htm#s5 (last access: 26 August 2021). The daily SLA/ADT maps with all
685 corrections applied are distributed via CMEMS (https://marine.copernicus.eu/; last access: 26
686 August 2021). Churchill River discharge data are provided in supplementary material. SLP and
687 wind data are available from the https://psl.noaa.gov/data/composites/hour/ and
688 https://psl.noaa.gov/cgi-bin/data/testdap/timeseries.pl (last access: 26 August 2021).

689

690 **Author contributions**

691 Conceptualization: ID; methodology: ID, DV, TS, AT; formal analysis: ID, DV, AT;
692 investigation: ID, DV, AC, TS; resources: KS, DBarber; data curation: ID, DV, AT; writing
693 (original draft): ID, DV, TS; writing (review & editing): AC, DV, SK, TS, AT, DBabb;
694 visualization: ID, DV; supervision: DBarber; project administration: KS, DBarber; funding
695 acquisition: KS, DBarber.

696

697 **Competing interests**

698 The authors declare that they have no conflict of interest.

699

700 **Acknowledgments**

701 This work is a part of research conducted under the framework of the Arctic Science Partnership
702 (ASP) and ArcticNet. This research is also a contribution to the Natural Sciences and
703 Engineering Council of Canada (NSERC) Collaborative Research and Development project:
704 BaySys (CRDPJ470028-14). Funding for this work was provided by NSERC, Manitoba Hydro,
705 the Canada Excellence Research Chair (CERC) program, the Canada Research Chairs (CRC)
706 program and the Canada-150 Research Chairs program. D. Babb is additionally supported by
707 NSERC and the Canadian Meteorological and Oceanographic Society (CMOS). DLV was
708 supported by NOAA Atlantic Oceanographic and Meteorological Laboratory under the auspices
709 of the Cooperative Institute for Marine and Atmospheric Studies (CIMAS), a cooperative
710 institute of the University of Miami and NOAA, cooperative agreement NA20OAR4320472.

711

712

References

Andrews, J., Babb, D., and Barber, D. G.: Climate change and sea ice: Shipping accessibility on the marine transportation corridor through Hudson Bay and Hudson Strait (1980 –2014), Elem. Sci. Anth., 5, 15, https://doi.org/10.1525/elementa.13, 2017.

CLS-DOS: Validation of altimeter data by comparison with tide gauge measurements: yearly report 2016, Ref. CLS-DOS-17-0016, available at: https://www.aviso.altimetry.fr/fileadmin/documents/calval/validation_report/annual_report_TG_ 2016.pdf, 2016, last access: 26 August 2021.

Copernicus Climate Change Service (C3S): ERA5: Fifth generation of ECMWF atmospheric reanalyses of the global climate. Copernicus Climate Change Service Climate Data Store (CDS), 2017, available at https://cds.climate.copernicus.eu/cdsapp#!/home, last access: 26 August 2021.

Déry, S. J., Stieglitz, M., McKenna, E. C., and Wood, E. F.: Characteristics and trends of river discharge into Hudson, James, and Ungava Bays, 1964–2000, J. Climate, 18, 2540–2557, https://doi.org/10.1175/JCLI3440.1, 2005.

Déry, S. J., Mlynowski, T. J., Hernández-Henríquez, M. A., and Straneo, F.: Interannual Variability and Interdecadal Trends in Hudson Bay Streamflow, Journal of Marine Systems, 88 (3), 341–351, https://doi.org/10.1016/j. jmarsys.2010.12.002, 2011.

Déry, S. J., Stadnyk, T. A., MacDonald, M. K., and Gauli-Sharma, B.: Recent trends and variability in river discharge across northern Canada, *Hydrology and Earth System Sciences*, 20, 4801–4818, https://doi.org/10.5194/hess-20-4801-2016, 2016.

Dmitrenko, I. A., Kirillov, S. A., and Tremblay, L. B.: The long-term and interannual variability of summer fresh water storage over the eastern Siberian shelf: Implication for climatic change, J. Geophys. Res., 113, C03007, https://doi.org/10.1029/2007JC004304, 2008a.

Dmitrenko, I. A., Kirillov, S. A., Tremblay, L. B., Bauch, D., and Makhotin, M.: Effects of atmospheric vorticity on the seasonal hydrographic cycle over the eastern Siberian shelf, Geophys. Res. Lett., 35, L03619, https://doi.org/10.1029/2007GL032739, 2008b.

Dmitrenko, I. A., Myers, P. G., Kirillov, S. A., Babb, D. G., Volkov, D. L., Lukovich, J. V., Tao, R., Ehn, J. K., Sydor, K., and Barber, D. G.: Atmospheric vorticity sets the basin-scale circulation in Hudson Bay, Elem. Sci. Anth., 8, 49, https://doi.org/10.1525/elementa.049, 2020.

Dmitrenko, I. A., Kirillov, S. A., Babb, D. G., Kuzyk, Z. A., Basu, A., Ehn, J. K., Sydor, K., and Barber D. G.: Storm-driven hydrography of western Hudson Bay, Continental Shelf Res., 227, 104525, https://doi.org/10.1016/j.csr.2021.104525, 2021.

Eastwood, R. A., McDonald, R., Ehn, J., Heath, J., Arragutainaq, L., Myers, P. G., Barber, D., and Kuzyk, Z. A.: Role of river runoff and sea-ice brine rejection in controlling stratification throughout winter in southeast Hudson Bay, Estuaries and Coasts, 43, 756–786, https://doi.org/10.1007/s12237-020-00698-0, 2020.

749 Fisher, R. A.: On the 'probable error' of a coefficient of correlation deduced from a small sample,
750 Metron, 1, 3–32, 1921.

751 Foreman, M. G. G.: Manual for tidal heights analysis and prediction, Pacific Marine Science
752 Report, 77–10, Patricia Bay, Sidney, BC, Institute of Ocean Sciences, 58 pp., 1977.

753 Godin, P., Macdonald, R. W., Kuzyk, Z. Z. A., Goñi, M. A., and Stern, G. A.: Organic matter
754 compositions of rivers draining into Hudson Bay: Present-day trends and potential as recorders
755 of future climate change, J. Geophys. Res. Biogeosci., 122, 1848–1869,
756 https://doi.org/10.1002/2016JG003569, 2017.

757 Gough, W. A.: Projections of sea-level change in Hudson and James Bays, Canada, due to global
758 warming, Arctic and Alpine Research, 30(1), 84-88, https://doi.org/10.2307/1551748, 1998.

759 Gough, W. A., and Robinson, C. A.: Sea-level Variation in Hudson Bay, Canada, from Tide-
760 Gauge Data, Arctic, Antarctic, and Alpine Research, 32(3), 331-335,
761 https://doi.org/10.1080/15230430.2000.12003371, 2000.

762 Gough, W. A., Robinson, C., and Hosseinian, R.: The Influence of James Bay River Discharge
763 on Churchill, Manitoba Sea Level, Polar Geography, 29(5), 213-223,
764 https://doi.org/10.1080/789610202, 2005.

765 Granskog, M. A., Macdonald, R. W., Kuzyk, Z. A., Senneville, S., Mundy, C.-J., Barber, D. G.,
766 Stern, G. A., and Saucier, F.: Coastal conduit in southwestern Hudson Bay (Canada) in summer:
767 Rapid transit of freshwater and significant loss of colored dissolved organic matter, J. Geophys.
768 Res., 114, C08012, https://doi.org/10.1029/2009JC005270, 2009.

769 Granskog, M. A., Kuzyk, Z. A., Azetsu-Scott, K., and Macdonald, R. W.: Distributions of
770 runoff, sea-ice melt and brine using δ18O and salinity data - A new view on freshwater cycling
771 in Hudson Bay, Journal of Marine Systems, 88, 362–374,
772 https://doi.org/10.1016/j.jmarsys.2011.03.011, 2011.

773 Guttenberg, B.: Changes in sea level, postglacial uplift, and mobility of the earth's interior,
774 Geological Society of America Bulletin, 52(5), 721–772, https://doi.org/10.1130/GSAB-52-721,
775 1941.

776 Hersbach, H., and Coauthors: The ERA5 global reanalysis, Quarterly Journal of the Royal
777 Meteorological Society, 146, 1999–2049, https://doi.org/10.1002/qj.3803, 2020.

778 Hochheim, K. P., and Barber, D. G.: Atmospheric forcing of sea ice in Hudson Bay during the
779 fall period, 1980–2005. J. Geophys. Res., 115, C05009, https://doi.org/10.1029/2009JC005334,
780 2010.

781 Hochheim, K. P., and Barber, D. G.: An update on the ice climatology of the Hudson Bay
782 System. Arctic Antarctic Alpine Res., 46(1), 66–83, https://doi.org/10.1657/1938-4246-46.1.66,
783 2014.

784 Ingram, R. G. and Prinsenberg, S.: Coastal oceanography of Hudson Bay and surrounding
785 Eastern Canadian Arctic Waters, In: Robinson, A. R. and K. N. Brink (Eds.), *The Sea*, Vol. 11.

786 The Global Coastal Ocean Regional Studies and Synthesis. Harvard University Press,
787 Cambridge, Massachusetts and London, 835–861, 1998.

788 Joyce, B. R., Pringle, W. J., Wirasaet, D., Westerink, J. J., Van der Westhuysen, A. J., Grumbine,
789 R., and Feyen, J.: High resolution modeling of western Alaskan tides and storm surge under
790 varying sea ice conditions, Ocean Modelling, 141, 101421,
791 https://doi.org/10.1016/j.ocemod.2019.101421, 2019.

792 Kalnay, E, Kanamitsu, M., Kistler, R., Collins, W., Deaven, D., Gandin, L., Iredell, M., Saha, S.,
793 White, G., Woollen, J., Zhu, Y., Chelliah, M., Ebisuzaki, W., Higgins, W., Janowiak, J., Mo, K.
794 C., Ropelewski, C., Wang, J., Leetmaa, A., Reynolds, R., Jenne, R., and Joseph D.: The
795 NCEP/NCAR 40-year reanalysis project, Bull. Am. Meteorol. Soc., 77, 437–471,
796 https://doi.org/10.1175/1520-0477(1996)077<0437: TNYRP>2.0.CO;2, 1996.

797 Kuzyk, Z. A., Macdonald, R.W., Stern, G. A., and Gobeil, C.: Inferences about the modern
798 organic carbon cycle from diagenesis of redox-sensitive elements in Hudson Bay, Journal of
799 Marine Systems, 88, 451–462, https://doi.org/10.1016/j.jmarsys.2010.11.001, 2011.

800 Kuzyk, Z. A. and Candlish, L. M.: From Science to Policy in the Greater Hudson Bay Marine
801 Region: An Integrated Regional Impact Study (IRIS) of Climate Change and Modernization,
802 ArcticNet, Québec City, 424 pp, 2019

803 Landy, J. C., Ehn, J. K., Babb, D. G., Theriault, N., and Barber D. G.: Sea ice thickness in the
804 eastern Canadian Arctic: Hudson Bay complex & Baffin Bay, Remote Sensing of Environment,
805 200, 281–294, https://doi.org/10.1016/j.rse.2017.08.019, 2017.

806 Larson, K. M., and van Dam, T.: Measuring postglacial rebound with GPS and absolute gravity,
807 Geophys. Res. Lett., 27, 3925–3928, https://doi.org/10.1029/2000GL011946, 2000.

808 Lüpkes, C., Gryanik, V. M., Hartmann, J., and Andreas, E. L.: A parametrization, based on sea
809 ice morphology, of the neutral atmospheric drag coefficients for weather prediction and climate
810 models, J. Geophys. Res. Atmospheres, 117, D13112, https://doi.org/10.1029/2012JD017630,
811 2012.

812 Mulet, S., Rio, M. H., Greiner, E., Picot, N., and Pascual, A.: New global Mean Dynamic
813 Topography from a GOCE geoid model, altimeter measurements and oceanographic in-situ data,
814 OSTST Boulder, USA, available at:
815 http://www.aviso.altimetry.fr/fileadmin/documents/OSTST/2013/oral/mulet_MDT_CNES_CLS
816 13.pdf, 2013, last access: 26 August 2021.

817 Pascual, A., Boone, C., Larnicol, G., and Le Traon, P.-Y.: On the quality of real-time altimeter
818 gridded fields: Comparison with in situ data, J. Atmos. Oceanic Technol., 26, 556–569,
819 https://doi.org/10.1175/2008JTECHO556.1, 2009.

820 Piecuch, C. G., and Ponte, R. M.: A wind-driven nonseasonal barotropic fluctuation of the
821 Canadian inland seas, Ocean Sci., 11, 175–185, https://doi.org/10.5194/os-11-175-2015, 2015.

822 Piecuch, C. G., and Ponte, R. M.: Nonseasonal mass fluctuations in the midlatitude North
823 Atlantic Ocean, Geophys. Res. Lett., 41, 4261–4269, https://doi.org/10.1002/2014GL060248,
824 2014.

825 Prinsenberg, S. J.: Freshwater contents and heat budgets of James Bay and Hudson Bay,
826 Continental Shelf Res., 3(2), 191-200, https://doi.org/10.1016/0278-4343(84)90007-4, 1984.

827 Prinsenberg, S. J.: Salinity and temperature distribution of Hudson Bay and James Bay, In:
828 Martini, E. P. (ed.) Canadian Inland Seas, Oceanogr. Ser. 44, Elsevier, New York, pp 163–186,
829 1986a.

830 Prinsenberg, S. J.: The circulation pattern and current structure of Hudson. In: Martini, E. P. (ed.)
831 Canadian Inland Seas, Oceanogr. Ser. 44, Elsevier, New York, 187–203, 1986b.

832 Prinsenberg, S. J.: Ice-cover and ice-ridge contributions to the freshwater contents of Hudson
833 Bay and Foxe Basin, Arctic, 41(1), 6–11, https://doi.org/10.14430/arctic1686, 1988.

834 Prinsenberg, S. J.: Effects of hydro-electric projects on Hudson Bay's marine and ice
835 environments, Potential Environ. Impacts Ser. 2, 8 pp., North Wind Inf. Serv., Montreal, 1991.

836 Pujol, M.-I., Faugère, Y., Taburet, G., Dupuy, S., Pelloquin, C., Ablain, M., and Picot, N.:
837 DUACS DT2014: the new multi-mission altimeter data set reprocessed over 20 years, Ocean
838 Sci., 12, 1067-1090, https://doi.org/0.5194/os-12-1067-2016, 2016.

839 Pew Charitable Trusts: The Integrated Arctic Corridors Framework. Planning for responsible
840 shipping in Canada's Arctic waters, available at:
841 https://www.pewtrusts.org/~/media/Assets/2016/04/The-Integrated-Arctic-Corridors-
842 Framework.pdf, 2016, last access: 26 August 2021.

843 Ray, R. D.: Sea Level, Land Motion, and the Anomalous Tide at Churchill, Hudson Bay,
844 American Geophysical Union, Fall Meeting 2015, abstract id. G43B-1040, 2015.

845 Ridenour, N. A., Hu, X., Sydor, K., Myers, P. G., and Barber, D. G.: Revisiting the circulation of
846 Hudson Bay: Evidence for a seasonal pattern, Geophysical Research Letters, 46, 3891–3899,
847 https://doi.org/10.1029/2019GL082344, 2019a.

848 Ridenour, N. A., Hu, X., Jafarikhasragh, S., Landy, J. C., Lukovich, J. V., Stadnyk, T. A., Sydor,
849 K., Myers, P. G., and Barber, D. G.: Sensitivity of freshwater dynamics to ocean model
850 resolution and river discharge forcing in the Hudson Bay Complex, Journal of Marine Systems,
851 196, 48-64, https://doi.org/10.1016/j.jmarsys.2019.04.002, 2019b.

852 Sella, G. F., Stein, S., Dixon, T. H., Craymer, M., James, T. S., Mazzotti, S., and Dokka, R. K.:
853 Observation of glacial isostatic adjustment in "stable" North America with GPS, Geophys. Res.
854 Lett., 34, L02306, https://doi.org/10.1029/2006GL027081, 2007.

855 Smith, C. A, Compo, G. P., and Hooper, D. K.: Web-based reanalysis intercomparison tools
856 (WRIT) for analysis and comparison of reanalyses and other datasets, Bull. Amer. Meteor. Soc.,
857 95(11): 1671–1678, https://doi.org/10.1175/BAMS-D-13-00192.1, 2014.

Saucier, F. J., and Dionne, J.: A 3-D coupled ice-ocean model applied to Hudson Bay, Canada: The seasonal cycle and time-dependent climate response to atmospheric forcing and runoff, J. Geophys. Res. Oceans, 103(C12), 27,689-27,705, https://doi.org/10.1029/98JC02066, 1998.

Saucier, F. J., Senneville, S., Prinsenberg, S., Roy, F., Smith, G., Gachon, P., Caya, D., and Laprise, R.: Modelling the sea ice-ocean seasonal cycle in Hudson Bay, Foxe Basin and Hudson Strait, Canada, Climate Dynamics, 23, 303–326, https://doi.org/10.1007/s00382-004-0445-6, 2004.

Schulze, L. M, and Pickart, R. S.: Seasonal variation of upwelling in the Alaskan Beaufort Sea: Impact of sea ice cover, J. Geophys. Res., 117, C06022, https://doi.org/10.1029/2012JC007985, 2012.

St-Laurent, P., Straneo, F., Dumais, J.-F., and Barber, D. G.: What is the fate of the river waters of Hudson Bay?, Journal of Marine Systems, 88, 352–361, https://doi.org/10.1016/j.jmarsys.2011.02.004, 2011.

Straneo, F., and Saucier, F.: The outflow from Hudson Strait and its contribution to the Labrador Current, Deep-Sea Res. I, 55, 926– 946, https://doi.org/10.1016/j.dsr.2008.03.012, 2008.

The Climate Change Initiative Coastal Sea Level Team. Coastal sea level anomalies and associated trends from Jason satellite altimetry over 2002–2018: Sci. Data, 7, 357, https://doi.org/10.1038/s41597-020-00694-w, 2020.

Tivy, A., Howell, S. E., Alt, B., Yackel, J. J., and Carrieres, T.: Origins and levels of seasonal forecast skill for sea ice in Hudson Bay using Canonical Correlation Analysis, J. Climate, 24(5), 1378-1395, https://doi.org/10.1175/2010JCLI3527.1, 2011.

Tsamados, M., Feltham, D. L., Schroeder, D., Flocco, D., Farrell, S. L., Kurtz, N., Laxon, S. W., and Bacon, S.: Impact of Variable Atmospheric and Oceanic Form Drag on Simulations of Arctic Sea Ice, J. Phys. Oceanography, 44(5), 1329–1353, https://doi.org/10.1175/JPO-D-13-0215.1, 2014.

Tushingham, A. M.: Observations of postglacial uplift at Churchill, Manitoba, Canadian Journal of Earth Sciences, 29, 2418-2425, https://doi.org/10.1139/e92-189, 1992.

Volkov, D. L., and Pujol, M.-I.: Quality assessment of a satellite altimetry data product in the Nordic, Barents, and Kara seas, J. Geophys. Res., 117, C03025, https://doi.org/10.1029/2011JC007557, 2012.

Volkov, D. L., Larnicol, G., and Dorandeu, J.: Improving the quality of satellite altimetry data over continental shelves, J. Geophys. Res., 112, C06020, https://doi.org/10.1029/2006JC003765, 2007.

Ward, P. J., Couasnon, A., Eilander, D., Haigh, I. D., Hendry, A., Muis, S., Veldkamp, T. I. E., Winsemius, H. C., and Wahl, T.: Dependence between high sea-level and high river discharge increases flood hazard in global deltas and estuaries, Environ. Res. Lett., 13, 084012, https://doi.org/10.1088/1748-9326/aad400, 2018.

895   Walsh, J. E., Chapman, W. L., and Shy, T. L.: Recent decrease of sea level pressure in the
896   central Arctic, J. Clim., 9, 480–486, https://doi.org/0.1175/1520-0442(1996)009<0480:
897   RDOSLP>2.0.CO;2, 1996.

898   Wang, J., L. Mysak, A. and Ingram, R. G.: A Three-Dimensional Numerical Simulation of
899   Hudson Bay Summer Ocean Circulation: Topographic Gyres, Separations, and Coastal Jets, J.
900   Phys. Oceanogr., 24, 2496–2514, https://doi.org/10.1175/1520-
901   0485(1994)024<2496:ATDNSO>2.0.CO;2, 1994.

902   Wolf, D., Klemann, V. and Wünsch, J.: A Reanalysis and Reinterpretation of Geodetic and
903   Geological Evidence of Glacial-Isostatic Adjustment in the Churchill Region, Hudson Bay, Surv.
904   Geophys., 27, 19–61, https://doi.org/0.1007/s10712-005-0641-x, 2006.

905 **Tables**

906 **Table 1:** Correlations (*R*) of daily atmospheric vorticity and/or Churchill River discharge against
907 ~~and~~ sea level anomalies in western Hudson Bay for the whole annual cycle

Predictor(s)/Time frame	1960 - 2019	Pre-diversion 1960 - 1976	Post-diversion 1977 - 2019
Vorticity	0.47	0.49	0.47
River discharge	0.22	0.20	0.23
Vorticity and river discharge*	0.53*	0.53*	0.53*

908

909 **Table 2:** Correlations (*R*) of monthly-mean atmospheric vorticity and/or Churchill River
910 discharge against ~~and~~ sea level anomalies in western Hudson Bay for the ice-free period (June-
911 November)

Predictor(s)/Time frame	1960 - 2019	Pre-diversion 1960 - 1976	Post-diversion 1977 - 2019
Vorticity	0.54	0.52	0.55
River discharge	0.08	0.03**	0.11
Vorticity and river discharge*	0.55*	0.52*	0.57*

912

913 **Table 3:** Correlations (*R*) of monthly-mean atmospheric vorticity and/or Churchill River
914 discharge against ~~and~~ sea level anomalies in western Hudson Bay for the ice-covered period
915 (December-May)

Predictor(s)/Time frame	1960 - 2019	Pre-diversion 1960 - 1976	Post-diversion 1977 - 2019
Vorticity	0.47	0.49	0.47
River discharge	0.21	0.12	0.19
Vorticity and river discharge*	0.52*	0.51*	0.52*

916

917 ***** The coefficient of multiple correlation is estimated based on the multiple linear regression
918 analysis

919 ****** Correlation not statistically significant at the 99% confidence level

920   **Figures**

921

922
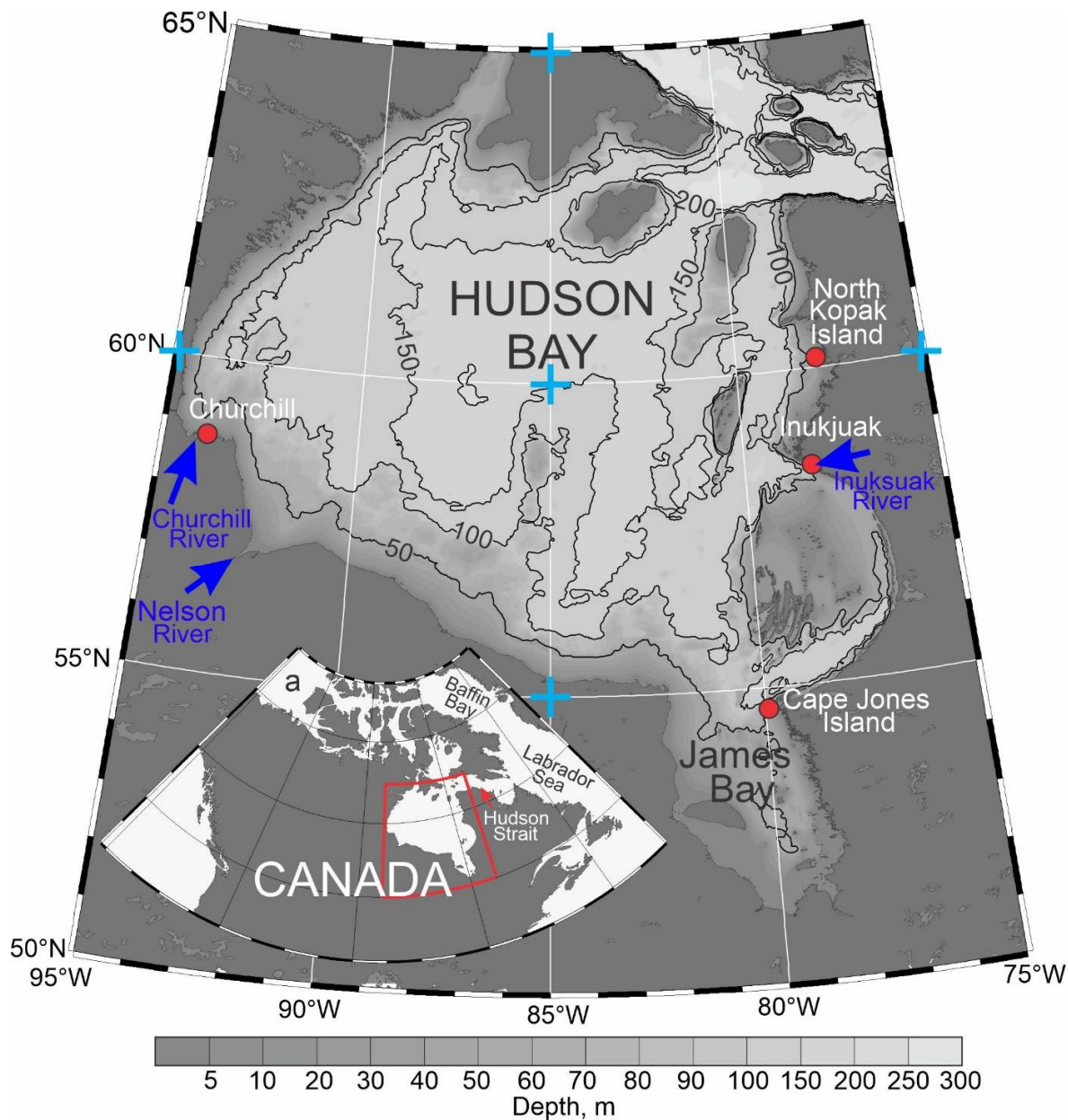
923

924   **Figure 1:** Map of Hudson Bay. Red dots depict the permanent tide gauge in Churchill and
925   temporary tide gauges in Innukjuak, Cape Jones Island and North Kopak Island. Blue arrows
926   highlight Churchill, Nelson and Inuksuak river mouths. Blue crosses depict the 5-point stencil
927   used for computing atmospheric vorticity approximated as Laplacian from sea level atmospheric
928   pressure. The numbered black lines depict depth contours of 50, 100, 150 and 200 m. (**a**) Inset
929   shows the Hudson Bay location within North America. The map of Hudson Bay was compiled
930   based on the General Bathymetric Chart of the Oceans (GEBCO, www.gebco.net).

931

932

933

934

935

936

937
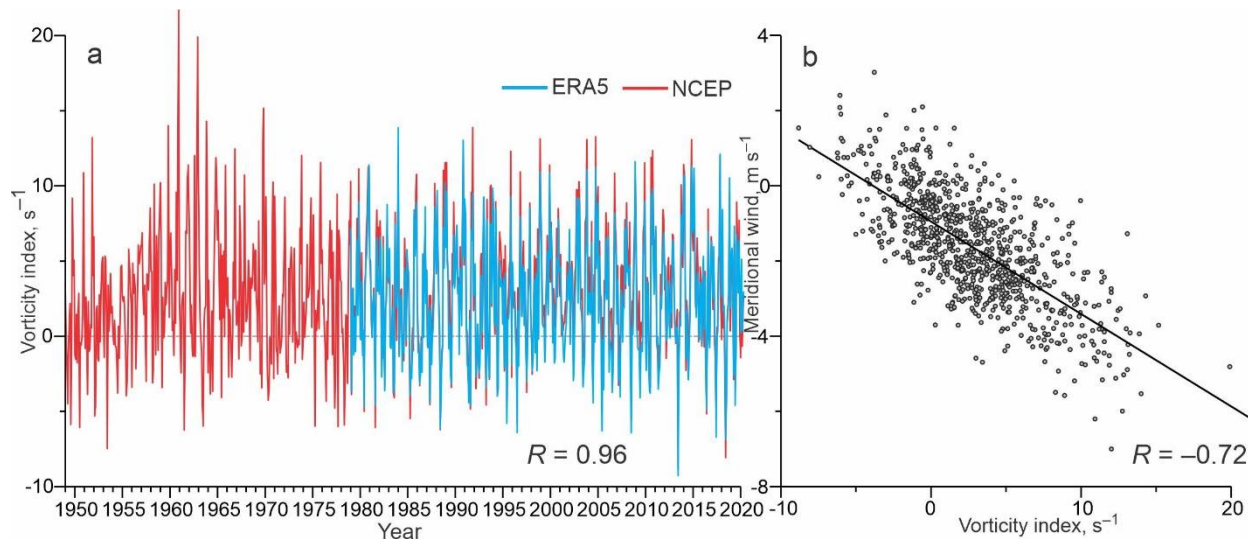
Figure 2: (**a**) Time series of the monthly mean atmospheric vorticity index (s^{-1}) over Hudson Bay, derived from NCEP (red) and ERA5 (blue). (**b**) Scatter plot of the monthly mean meridional wind seaward of Churchill in western Hudson Bay (m s^{-1}) versus the monthly mean atmospheric vorticity index. Thick black line depicts linear regression. Numbers at the bottom show correlation R between (**a**) the monthly mean vorticity derived from NCEP (1949-2000) and ERA5 (1979-2000) and (**b**) the monthly mean NCEP vorticity versus meridional wind (1949-2020).

945

946
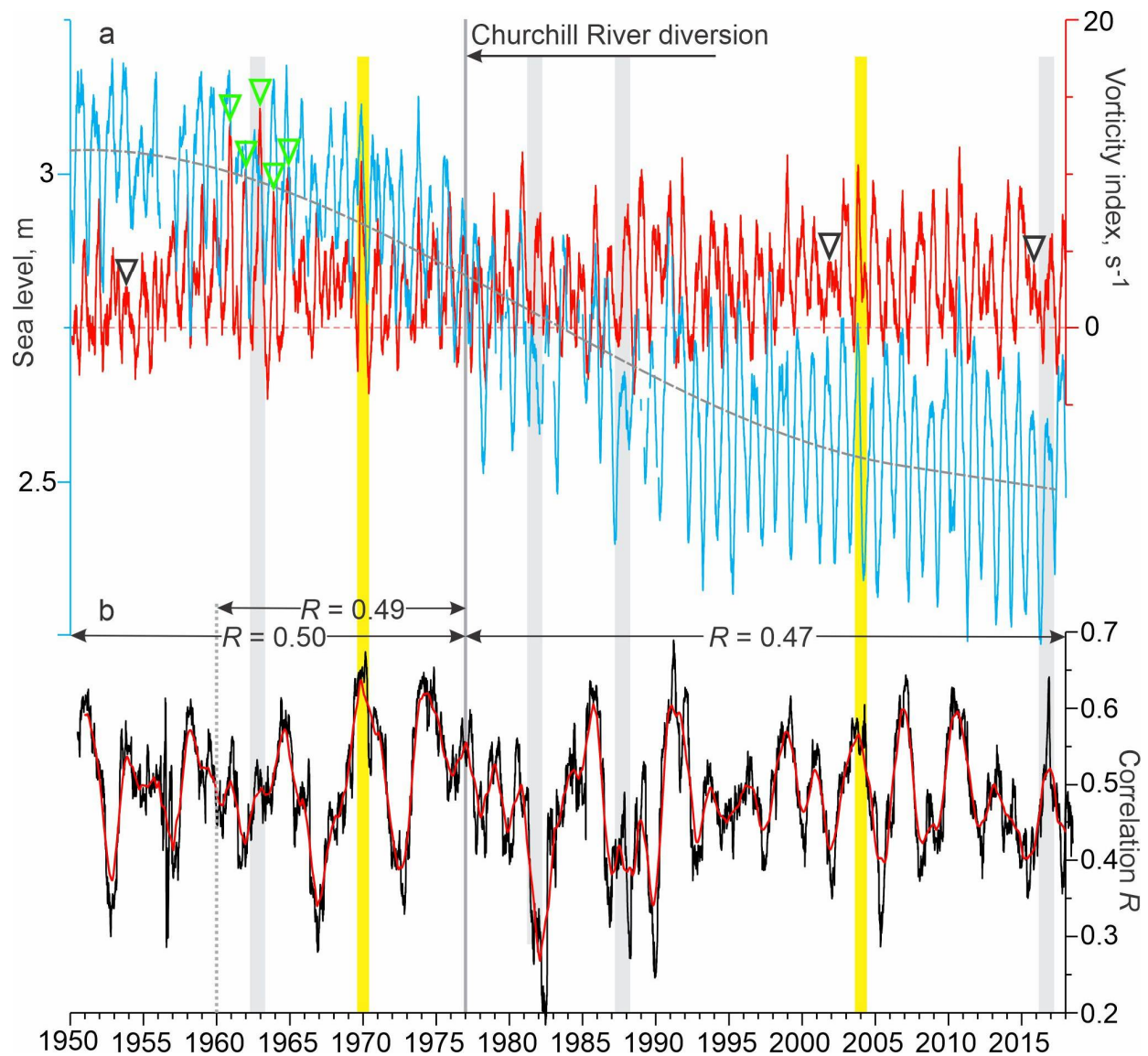
Figure 3: (**a**) 91-day running mean of daily mean atmospheric vorticity index (red, s^{-1}) over Hudson Bay and sea level measured at the tide gauge in Churchill (blue, m). Positive and negative vorticity correspond to cyclonic and anticyclonic atmospheric circulation, respectively. Gray dashed line shows polynomial approximation of the sea level trend attributed to the glacial isostatic adjustment. Black and green triangles show periods when seasonal vorticity from late fall to early winter was diminished and amplified, respectively. (**b**) Correlation R between daily vorticity index and sea level anomaly (SLA) computed for the 365-day moving window (black) with their 365-day running mean (red). All correlations are statistically significant at 99% confidence. Numbers at the top show correlation between daily vorticity index and SLA computed for 1950/60-1976 and 1977-2018 pre- and post-diversion, respectively. (**a, b**) Yellow shading highlights August-May 1969-70 and 2003-04, enlarged in Figure 6. Black arrow indicates onset of the Churchill River diversion. Gray shading highlights periods when the sea level seasonal cycle was partially disrupted (1981-82 and 1987-88), or significantly diminished (1962-63 and 2016-2017).

961
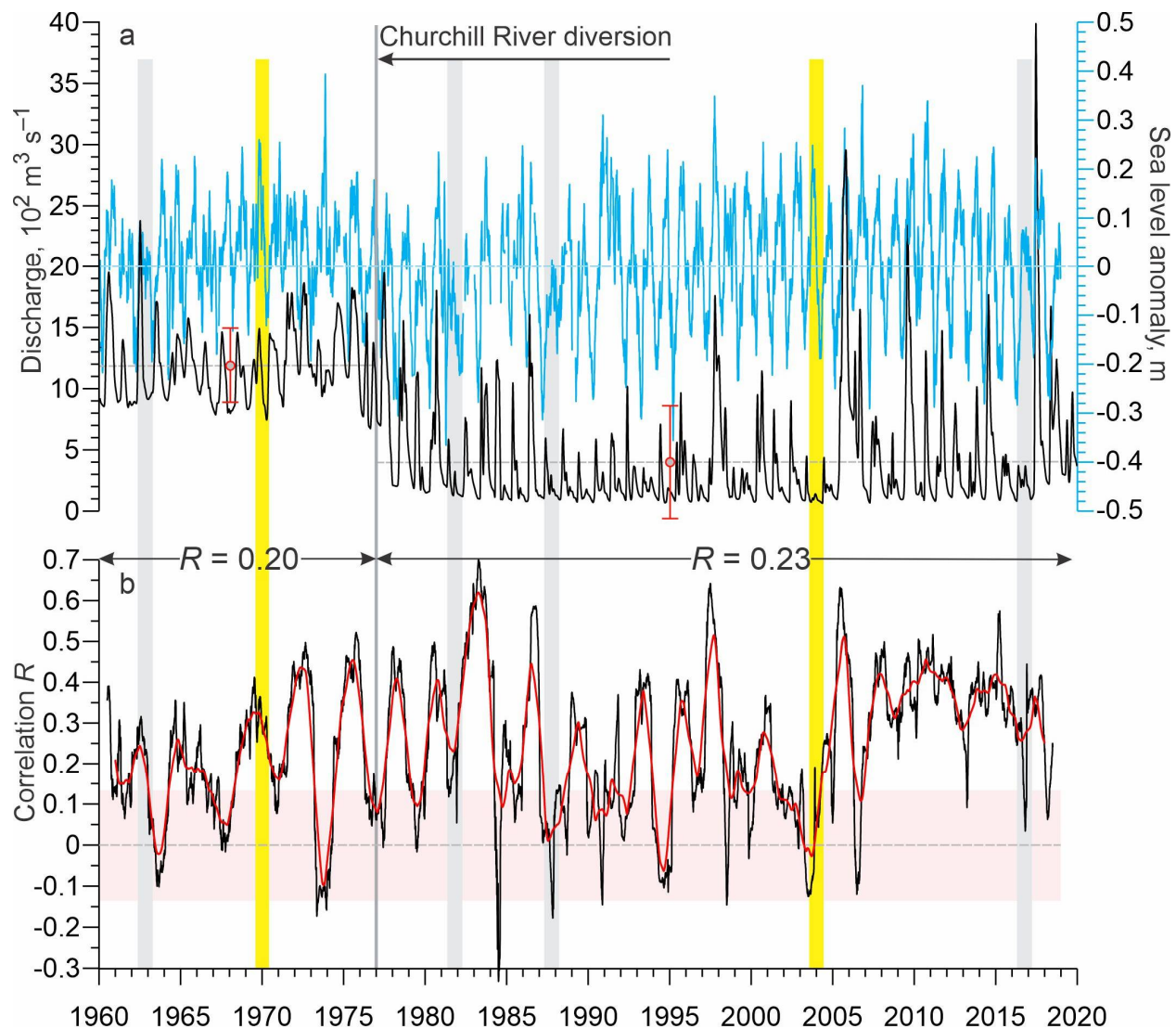
962

963

964 **Figure 4:** (**a**) 30-day running mean of the Churchill River discharge (black; 10^2 m^3 s^{-1}) and
965 detrended SLA at Churchill (blue; m). Gray circles show mean discharge pre- and post-diversion
966 with standard deviations depicted with red error bars. (**b**) Correlation *R* between daily Churchill
967 River discharge and SLA computed for the 365-day moving window (black) with their 365-day
968 running mean (red). Pink shading highlights statistically insignificant correlations at the 99%
969 confidence level. Numbers at the top show correlation between daily Churchill River discharge
970 and SLA computed for 1950-1976 and 1977-2018 pre- and post-diversion, respectively. (**a, b**)
971 Yellow shading highlights August-May 1969-70 and 2003-04. Black arrow indicates onset of the
972 Churchill River diversion. Gray shading highlights periods when the sea level seasonal cycle was
973 partially disrupted (1981-82 and 1987-88), or significantly diminished (1962-63 and 2016-2017).

974

975
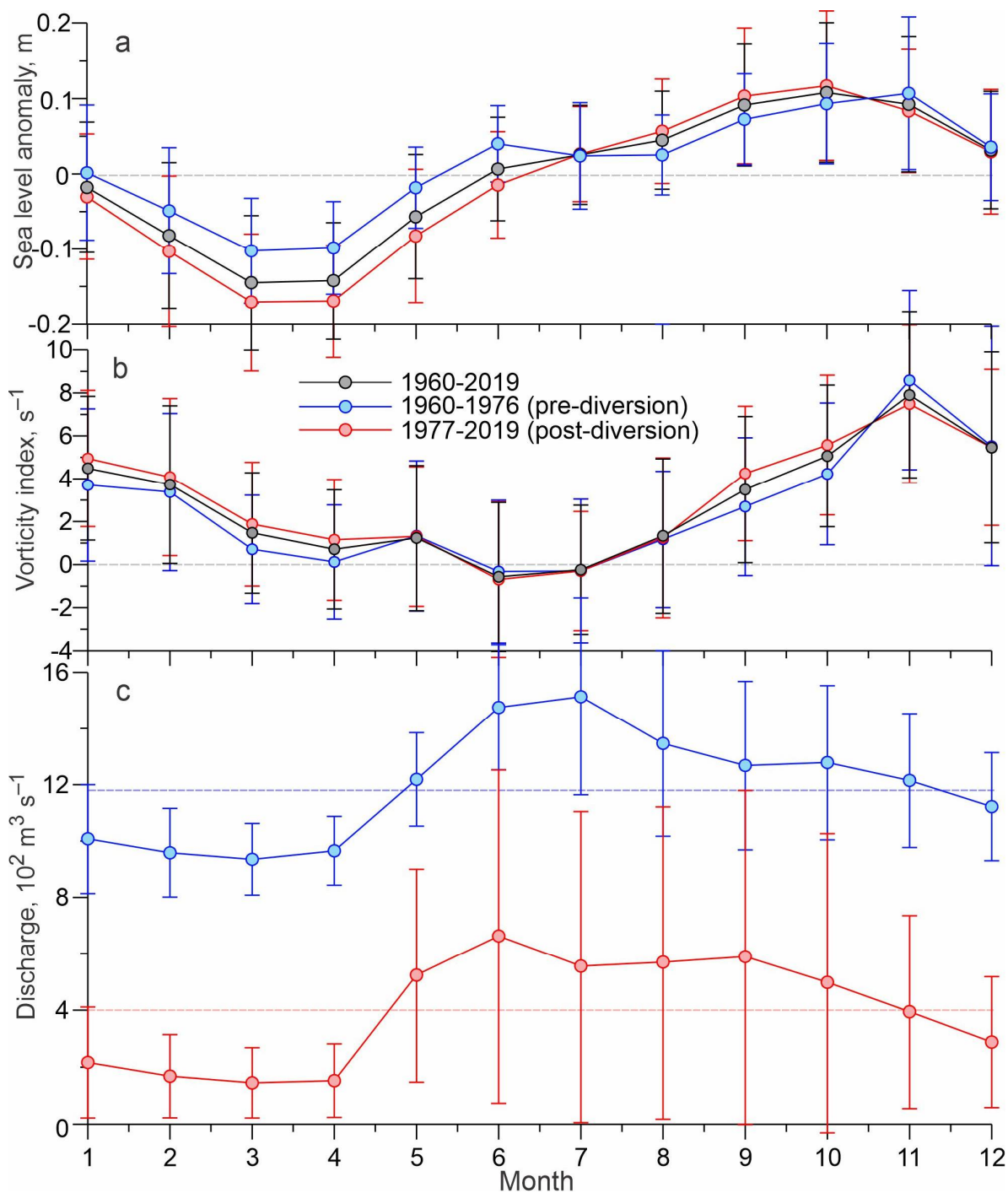
Figure 5: Seasonal cycle of (**a**) SLA at Churchill (m), (**b**) atmospheric vorticity over Hudson
Bay (s^{-1}), and (**c**) Churchill River discharge (10^2 m^3 s^{-1}). Seasonal cycle derived using monthly-
mean data for (**a, b**) 1950-2019 (black), (**a, b**) 1950-76 (blue) and (**c**) 1960-76 (blue) before the
Churchill River diversion, and (**a, b, c**) 1977-2018 (red) after the Churchill River diversion. Error
bars show ± one standard deviation of the mean. (**c**) Blue and pink dashed lines show the long-
term mean discharge before and after diversion, respectively.

982
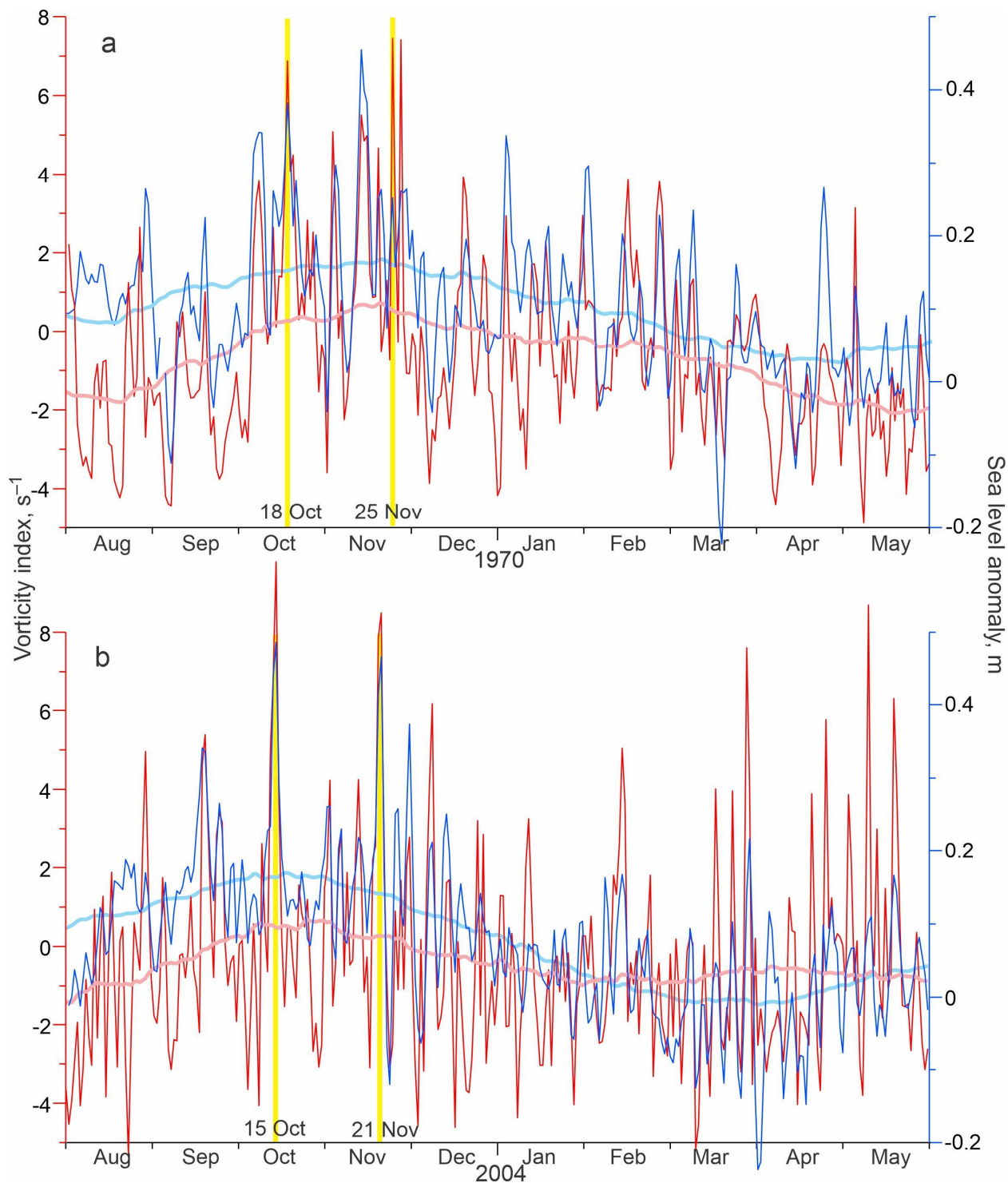
Figure 6: Time series of the daily mean vorticity index (red; s^{-1}) and SLA at Churchill (blue; m) with their 91-day running mean in pink and light blue, respectively, for August/May (**a**) 1969/1970 and (**b**) 2003/2004. (**a, b**) Vertical yellow lines highlight coherent peaks in vorticity and sea level in October and November.

988

989

990

991

992

993
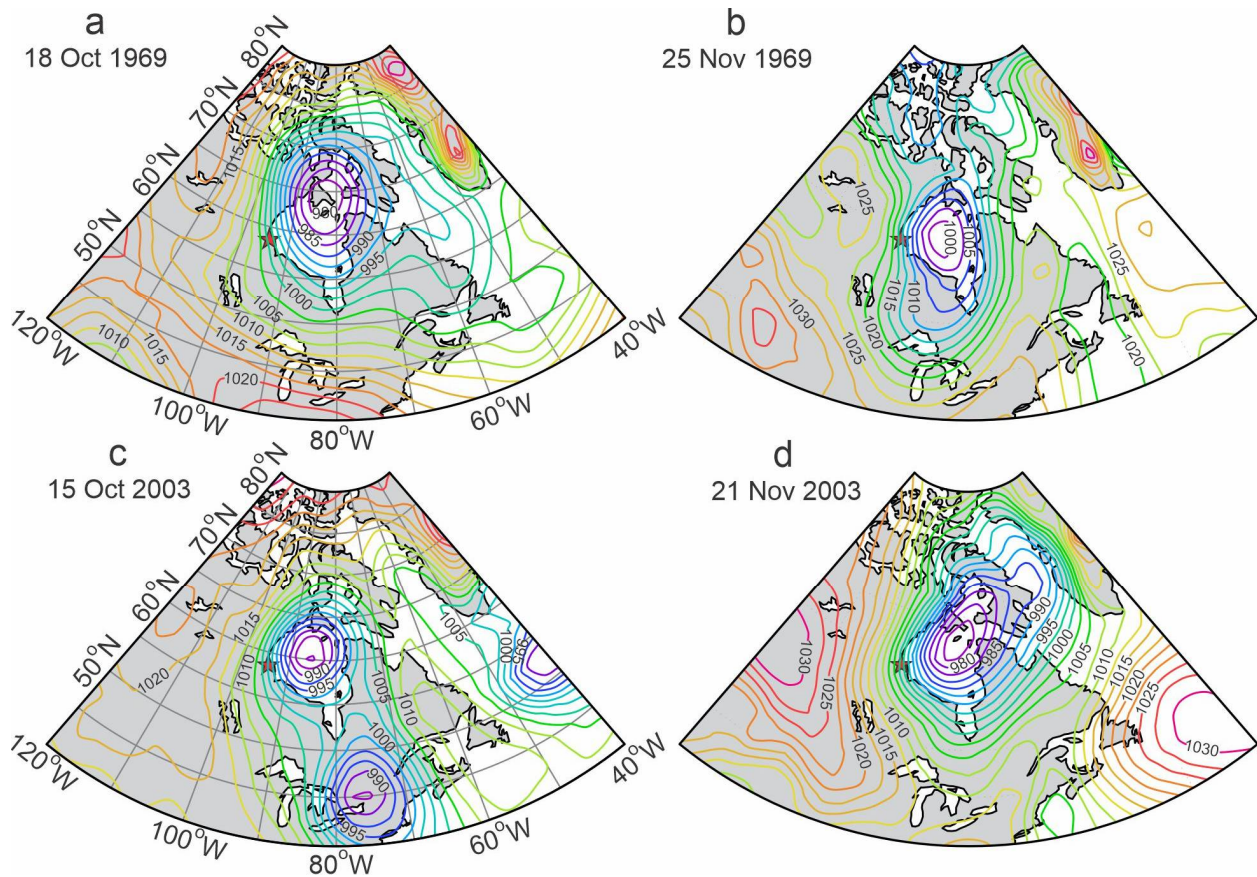
Figure 7: Sea level atmospheric pressure (hPa) for coherent peaks in atmospheric vorticity and sea level at Churchill, highlighted in Figure 6 with yellow lines: (**a**) 18 October 1969, (**b**) 25 November 1969, (**c**) 15 October 2003, and (**d**) 21 November 2003.

997

998

999

1000

1001

1002

1003

1004
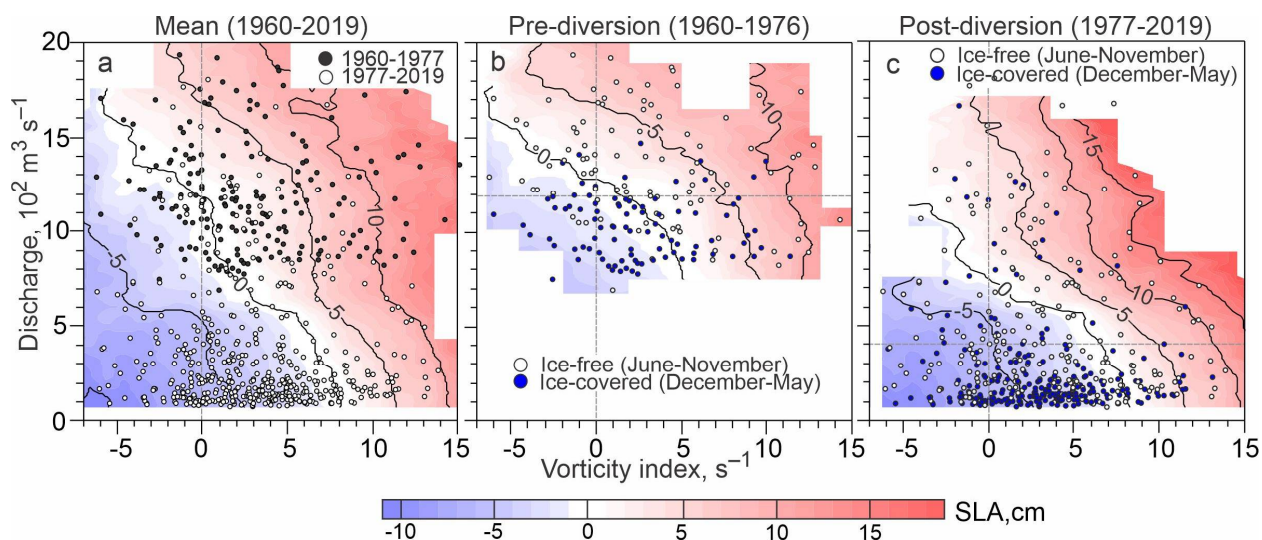
1005

Figure 8: Color shading shows monthly mean sea level anomalies (cm) from tidal gauge at Churchill versus atmospheric vorticity (s^{-1}; horizontal axis) and Churchill River discharge (10^2 m^3 s^{-1}; vertical axis) for (**a**) entire period of river discharge observations (1960 – 2019), and (**b**) before and (**c**) after the Churchill River diversion in 1977. Scatter plots show monthly mean vorticity and river discharge for (**a**) 1960-1976 (black circles) and 1977-2019 (white circles), and (**b, c**) ice-free season (June-November; white circles) and ice-covered season (December-May; blue circles). Horizontal gray dashed line shows mean river discharge (**c**) before and (**d**) after diversion.

1014

1015

1016

1017

1018

1019

1020

1021
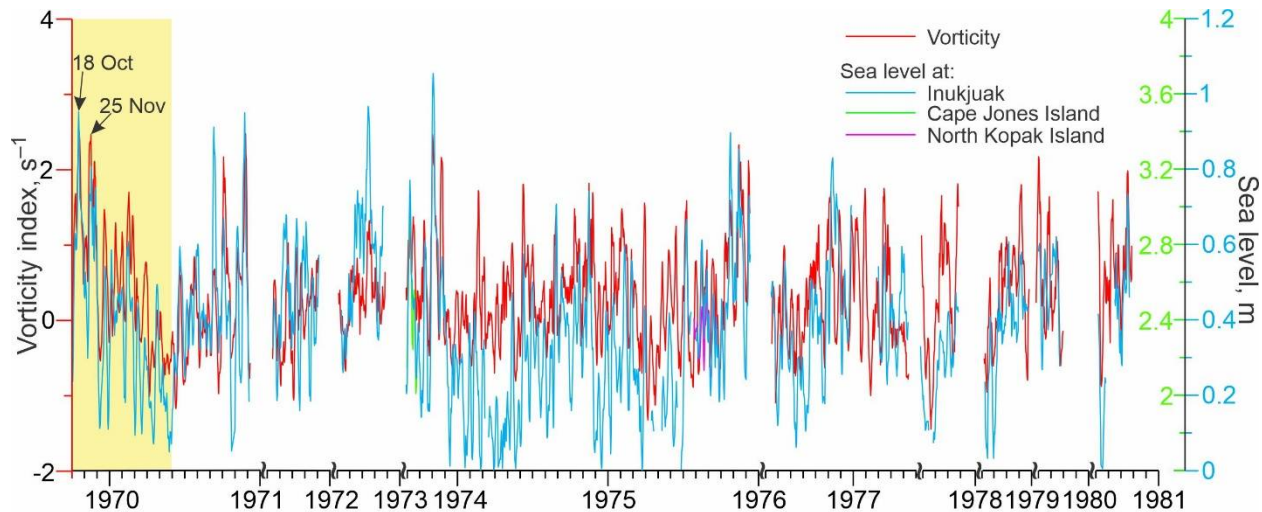
1022

Figure 9: Time series of 7-day running mean for daily atmospheric vorticity index (red, s⁻¹) over Hudson Bay and daily mean sea level (m) measured at the tide gauge in Innukjuak (blue), Cape Jones Island (green) and North Kopak Island (purple). Yellow shading highlights October/May 1969/70. Black arrows indicate two cyclonic storms in 18 October and 25 November 1969 with atmospheric forcing shown in Figures 7a and 7b, respectively. Right vertical axis shows sea-level scale for Innukjuak (blue), and Cape Jones Island and North Kopak Island (green).

1029

1030

1031

1032

1033
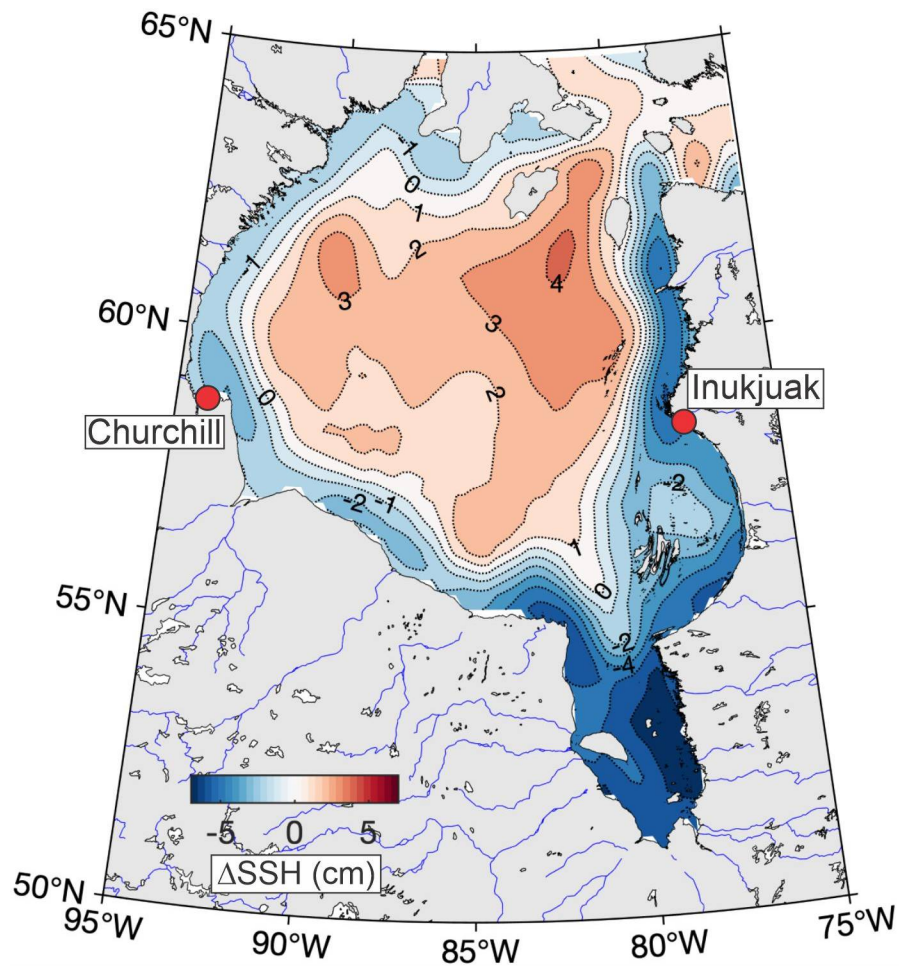
1034

Figure 10: The long-term mean (1993-2020) difference between sea surface height (SSH; cm) in summer (June-August) and fall (September-November) derived from the satellite altimetry. Red dots depict the tide gauge in Churchill and Innukjuak.

1038

1039

1040

1041

1042

1043

1044
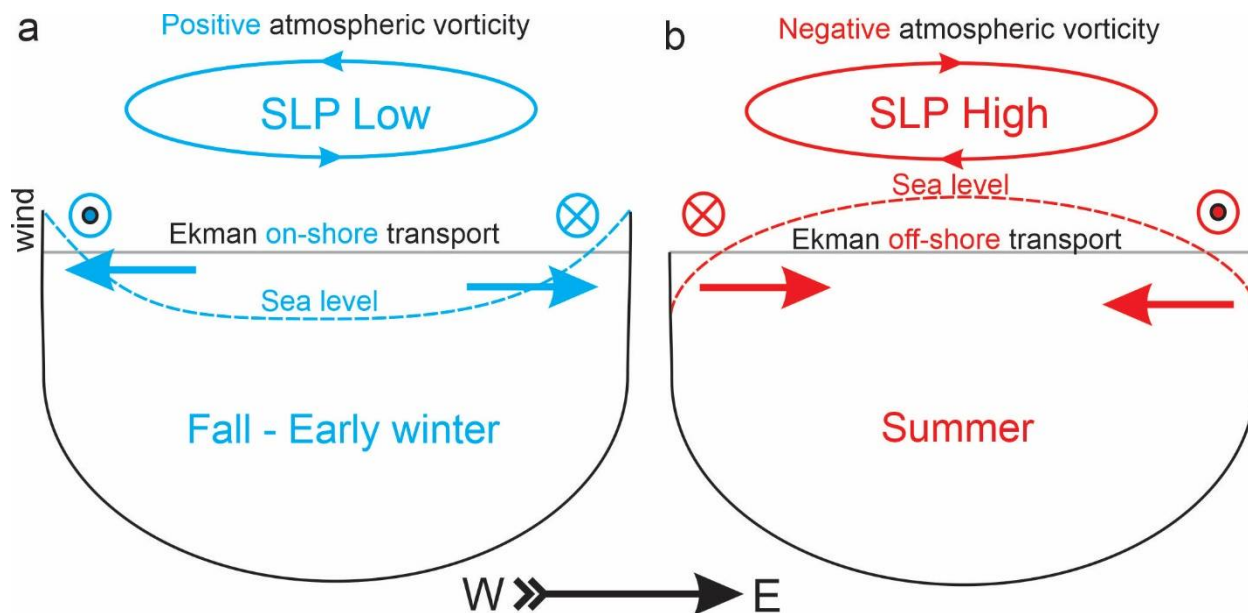
1045

Figure 11: Diagram of the proposed impact of the seasonal changes in atmospheric vorticity on the sea level seasonal variability in Hudson Bay. (**a**) Positive (cyclonic) vorticity during October-December causes onshore Ekman transport and storm surges over the coast. (**b**) Negative (anticyclonic) vorticity during June-July forces offshore Ekman transport. During winter, a complete sea-ice cover reduces momentum transfer from wind stress to the water column diminishing impact of atmospheric forcing on sea level variability. Dotted and crossed circles depict southerly and northerly along-shore surface winds, respectively.

1053